

## Seasonality of spectral albedo and transmittance as observed in the Arctic Transpolar Drift in 2007

Marcel Nicolaus,<sup>1,2</sup> Sebastian Gerland,<sup>1</sup> Stephen R. Hudson,<sup>1</sup> Susanne Hanson,<sup>3</sup> Jari Haapala,<sup>4</sup> and Donald K. Perovich<sup>5</sup>

Received 21 December 2009; revised 25 May 2010; accepted 11 June 2010; published 16 November 2010.

[1] The first continuous and high temporal resolution record of spectral albedo and transmittance of snow and sea ice in the Arctic Ocean over an entire summer season is presented. Measurements were performed at a manned station on multiyear sea ice in the Transpolar Drift during the drift of the schooner *Tara* from April to September 2007. Concurrent autonomous measurements of ice mass balance and weekly observations of snow and sea-ice properties complement the data set. The seasonality of physical and biological processes of snow and sea ice is characterized, including quantification of melt onset (10 June), melt season duration, and freeze onset (15 August). Over one year, approximately two thirds of the transmitted energy reached the ocean during the 66-day-long melt season. During the second half of July, transmitted irradiance decreased by 90% and absorption in and directly under the ice increased, significantly affecting the vertical partitioning of irradiance. The spectral radiation time series suggests that high biomass abundance in or below the sea ice caused this decrease. Comparing the spectral data set with broadband albedo data measured at the same location shows that 90% of the temporal variability of broadband albedo can be explained by variability in spectral albedo integrated over the limited wavelength range. The combination of spectral radiation and ice mass balance measurements allows a comprehensive description, and quantification, of snow and sea-ice processes, even with minimal additional in situ observations, suggesting such data sets can be collected autonomously to provide insight into the physical and biological processes on sea ice.

**Citation:** Nicolaus, M., S. Gerland, S. R. Hudson, S. Hanson, J. Haapala, and D. K. Perovich (2010), Seasonality of spectral albedo and transmittance as observed in the Arctic Transpolar Drift in 2007, *J. Geophys. Res.*, 115, C11011, doi:10.1029/2009JC006074.

### 1. Introduction

[2] The pack ice of the Arctic Ocean has experienced significant changes during the last decades. The most apparent changes are observed in the average and annual minimum sea-ice extent [e.g., Comiso *et al.*, 2008; Parkinson and Cavalieri, 2008; Stroeve *et al.*, 2008]. But sea-ice thickness has also decreased [e.g., Giles *et al.*, 2008; Haas *et al.*, 2008; Kwok and Rothrock, 2009] and the residence time of sea ice in the Arctic has decreased [e.g., Gascard *et al.*, 2008; Maslanik *et al.*, 2007; Rampal *et al.*, 2009]. Altogether, a shift from thicker multiyear ice (MYI) to thinner first-year ice (FYI) has been observed [Haas *et al.*, 2008;

Maslanik *et al.*, 2007; Nghiem *et al.*, 2007]. The observed changes in the ice cover were stronger than those projected by climate models [Stroeve *et al.*, 2007; Wang and Overland, 2009].

[3] One of the most important feedback processes related to snow and sea ice results from the ability of these surfaces to reflect most short-wave irradiance back to the atmosphere and the relationship between this ability and temperature: warming the snow and ice causes a decrease in albedo, leading to further warming [Curry *et al.*, 2001; Morassutti, 1991]. This ice-albedo feedback has been studied extensively by measurements of incident and reflected (back-scattered) irradiance and observations of physical surface properties [e.g., Aoki *et al.*, 2003, 2000; Grenfell and Perovich, 1984; Perovich, 1996; Perovich *et al.*, 2002a; Warren, 1982]. During winter and early spring, most of the solar short-wave irradiance is reflected and backscattered from the surface. This fraction decreases as snow grain size increases [Bohren and Barkstrom, 1974; Grenfell and Perovich, 1984; Perovich, 2005; Warren, 1982], snow thickness decreases [Baker *et al.*, 1991; Brandt *et al.*, 2005], and melt ponds form during summer [e.g., Fetterer and

<sup>1</sup>Norwegian Polar Institute, Tromsø, Norway.

<sup>2</sup>Now at Alfred Wegener Institute for Polar and Marine Research, Bremerhaven, Germany.

<sup>3</sup>Danish Meteorological Institute, Copenhagen, Denmark.

<sup>4</sup>Finnish Meteorological Institute, Helsinki, Finland.

<sup>5</sup>Cold Regions Research and Engineering Laboratory, Hanover, New Hampshire, USA.

Untersteiner, 1998; Perovich et al., 2002a, 2002b, 2003]. Consequently, more irradiance reaches the deeper snow layers as well as the sea ice and upper ocean underneath as the melt season progresses.

[4] Spectral albedo measurements enable more detailed analyses of snow and sea-ice properties than do broadband albedos. Analyzing albedo spectra allows different processes to be described without performing additional in situ measurements, on the basis of those processes' known affect on spectral albedo. Furthermore, seasonal data sets of spectral albedo are needed for validation and calibration of optical and microwave remote sensing instruments. However, time series data of spectral albedo are sparse because it is technically and methodologically difficult to measure them accurately and with high temporal resolution.

[5] The most comprehensive study of the transmittance of snow and sea ice was performed by *Light et al.* [2008] on FYI and MYI during the Surface Heat Budget of the Arctic Ocean (SHEBA) drift experiment in 1998. In addition, several studies have focused on deriving absorption and/or scattering coefficients for different types of snow and sea ice [e.g., *Grenfell and Maykut*, 1977; *Grenfell et al.*, 2006; *Perovich*, 1996; *Perovich et al.*, 1998; *Weeks and Ackley*, 1986]. Those studies contributed to the description of how solar radiation contributes to internal and basal warming and melting of sea ice. Nevertheless, energy fluxes through snow and sea ice are still not well quantified, even though *Perovich* [2005] demonstrated their importance, estimating that light penetration through bare and ponded ice accounts for 23% and 16%, respectively, of the solar energy input into the ocean at SHEBA. Relatively little is known about the vertical partitioning of solar radiation, the amount of energy absorbed in sea ice, transmitted into sea-ice bottom layers, and transmitted into the upper ocean, and its high lateral variability [*Perovich et al.*, 1998]. But quantifying these processes is critical for understanding atmosphere-ice-ocean interaction, and how it might change in the future.

[6] Connections between physical, biological, and optical properties of sea ice have been long recognized [*Grenfell and Maykut*, 1977; *Maykut and Grenfell*, 1975]. The amount and seasonal timing of energy fluxes into and through sea ice are of critical importance for biological and biogeochemical processes at the ice underside and in the uppermost ocean. Light is known to be one of the most important factors limiting biological primary production and activity [e.g., *Arrigo*, 2003; *Lavoie et al.*, 2005], while at the same time algal layers affect attenuation coefficients, reducing transmittance to lower layers [*Perovich et al.*, 1998]. *Legendre and Gosselin* [1991], *Mundy et al.* [2007], and *Perovich et al.* [1993] have used spectral transmittance measurements to separate the effects of snow and algae on transmittance and to develop a method for non-destructive estimates of biomass in and under sea ice. Recent studies by *Ehn et al.* [2008a, 2008b] have combined field observations with numerical studies in order to derive diffuse attenuation coefficients for different ice types, and relating them to chlorophyll *a* concentrations and detritus.

[7] Previously, most measurements of spectral radiation were limited to spot measurements and short time periods. Despite all the needs for such data, high-resolution time series measurements of these properties are not widely available, mostly because such observations must overcome

several technical and logistical challenges, including keeping sensors clean and leveled.

[8] Here we present a continuous record of spectral albedo and transmittance of snow and sea ice in the Arctic Ocean over an entire summer season. Simultaneous measurements from an ice mass balance buoy (IMB) and weekly observations of snow and sea-ice properties by crew members complement the data set and enable joint analyses. The measurements were performed on multiyear sea ice in the Transpolar Drift between 86.5° and 88.5°N during the drift of the schooner *Tara* from April to September 2007, just before the record minimum Arctic sea-ice extent was observed.

## 2. Field Measurements

### 2.1. *Tara* Drift

[9] All measurements were performed during the drift of the schooner *Tara* as part of an integrative study during the EU-funded project Developing Arctic Modeling and Observing Capabilities for Long-Term Environmental Studies [*Gascard et al.*, 2008]. *Tara* was frozen into the ice north of the Laptev Sea (79.5°N, 143°E) on 4 September 2006, emulating the *Fram* expedition of 1893–1896. Figure 1 shows the entire drift (blue line) until the schooner left the ice again in the Fram Strait after 505 drifting days on 21 January 2008. While scientific measurements were performed during most of the drift, the most extensive observation period started with a 1 week field campaign from 22 to 29 April 2007 and lasted until early September 2007. *Tara* drifted approximately twice as fast as *Fram*, moved along by a comparatively strong tailwind [*Vihma et al.*, 2008].

### 2.2. Spectral Irradiance Measurements

[10] Spectral irradiance measurements were performed with Ramses ACC-2 VIS hyperspectral radiometers, covering a wavelength range from 320 to 950 nm with an average spectral resolution of 3.3 nm. All data were recorded at 30 min intervals with a data logger. The sensors, the data logger, and their use for irradiance studies over and under sea ice are described in detail by *Nicolaus et al.* [2010].

[11] The presented spectral irradiance measurements were performed in parallel with broadband short- and long-wave irradiance measurements by a group from the University of Tartu, Estonia [*Vihma et al.*, 2008]. All above-ice sensors were mounted on the same rack, which was fixed to wooden poles frozen into the ice, to reduce tilt due to surface melting. All sensors were adjusted and leveled independent from the rack itself. The station was set up on level ice about 100 m from *Tara*, far enough to prevent significant influences from activities on board or from the ship itself, but close enough to enable easy access for maintenance and to reduce the risk of losing the station.

[12] Figure 2 shows the albedo setup, consisting of one upward-looking (measuring incident irradiance,  $F_I(\lambda, t)$ ) and one downward-looking (measuring reflected irradiance,  $F_R(\lambda, t)$ ) radiometer. The upward-looking sensor included additional inclination and pressure sensors. The downward-looking sensor was approximately 2 m above the snow surface and 0.4 m horizontally from the rack.  $F_R$  was corrected for shadow effects independent of wavelength and time with a scaling factor of 1.0769, as described by

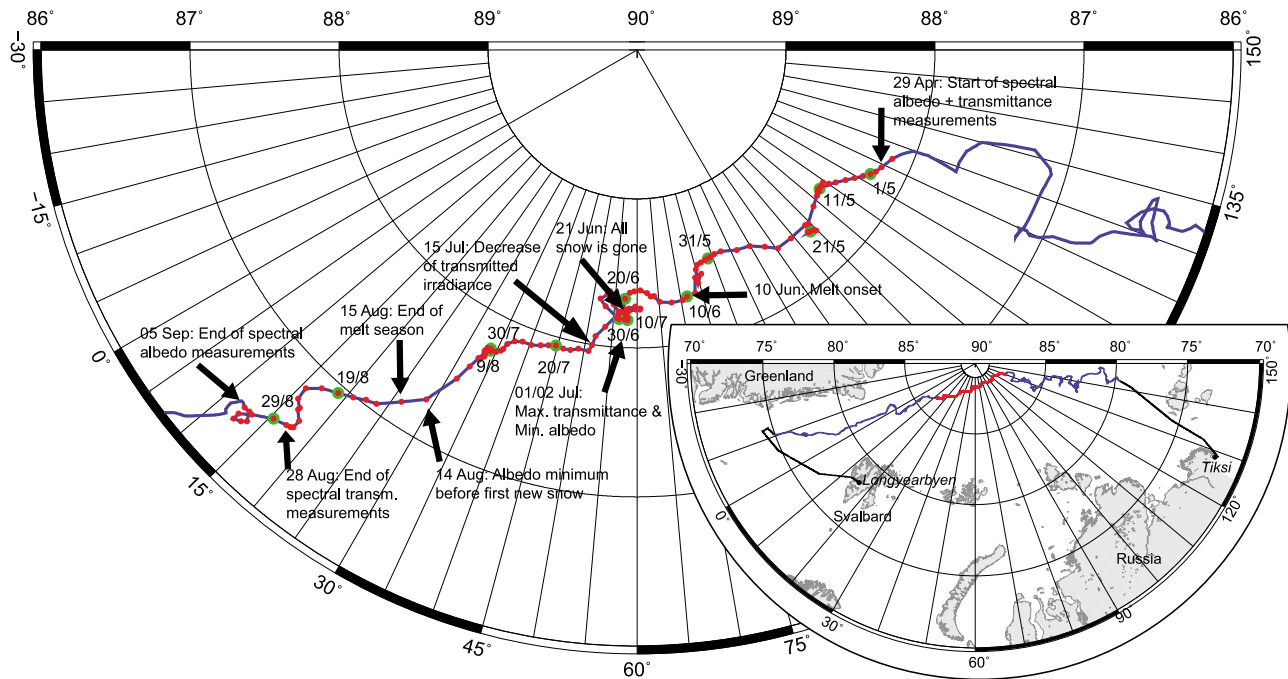


**Figure 1.** Map of *Tara* drift during spectral irradiance measurements (main figure) and map of the entire voyage of *Tara* from Tiksi, Russia, to Longyearbyen, Svalbard (inlay). The blue line shows the drift track and red dots give daily positions of *Tara* at the time of highest sun elevation (Figure 4d); green dots and text labels mark every 10th day for better orientation. Sailing transects are shown as black lines (inlay figure only). Additionally, significant events are labeled (Table 1).

Nicolaus et al. [2010].  $F_T$  was not affected by any obstacles at any time; hence corrections were not necessary. During installation and maintenance, we tried to avoid stepping on the snow surface under the sensors. Initial snow thickness was 0.1 m (28 April 2007), representative of the area around the station. The under-ice sensor was located  $\sim 10$  m from the main rack. The sensor was looking upward to measure transmitted irradiance ( $F_T(\lambda, t)$ ), mounted in a 13-cm-diameter metal frame deployed through a 20-cm-diameter borehole (Figure 2). After deployment, the surface around the sensor was restored as well as possible, while the borehole refroze with time.  $F_T$  was corrected for the shadow of the frame and suspension, independent of wavelength and time, with a scaling factor of 1.0804, as described by Nicolaus et al. [2010]. At the beginning of the observations, ice thickness was 2.0 m, the freeboard 0.1 m, and snow thickness 0.1 m, and the sensor was hanging 1.4 m under the ice bottom (3.3 m under the surface water level). Pressure, proportional to depth in water, and inclination were also measured by the sensor. On the basis of these data, it was found that the under-ice sensor dropped from 1.4 to 1.9 m on 17 July and continued dropping to a final depth of 2.8 m under the original ice underside after 5 August (depth data not shown here). This change was most likely due to surface melt processes and warming of the ice, which allowed the anchoring lines and cables to cut into the ice and release some slack. Transmittance spectra were corrected for these depth changes to make all spectra representative of the original depth, 1.4 m under the ice. For the correction, an absorption spectrum of seawater was extracted from the measurements and scaled with the change in depth. For details, see Nicolaus et al. [2010]. Inclination of the sensor

was not affected by these movements. Spectral irradiance measurements started on 28 April 2007 at 2230 UTC. The under-ice sensor had to be retrieved after 122 days of recording on 28 August 2007 at 1400 UTC. In total, 5838 transmittance spectra were recorded. Albedo measurements continued for another 8 days until 5 September 2007 at 0830 UTC, because the retrieval of the albedo sensors was much easier, less time consuming, and less weather dependent. In total, 6213 spectra of albedo were recorded. During the entire observation period, the station was visited daily, in order to check both the leveling of the station and the condensation or icing on the sensors. Surprisingly, the spectral radiometers were not found to be covered by frost or rime during any inspection, and did not have to be cleaned at all. It might be that night or early morning data were affected by condensation on the sensors, but this moisture evaporated very soon afterward [see also Nicolaus et al., 2010]. The sensors also did not have to be leveled during the entire observation period, because the wooden base of the station remained firmly frozen to the sea ice (T. Palo, personal communication, 2008). The under-ice sensor was not maintained in any way; maintenance would have been nearly impossible without destroying the entire setup.

[13] All observations were performed during polar day and the solar elevation angle ( $90^\circ - \text{solar zenith angle}$ ) varied between  $3^\circ$  (5 September) and  $25^\circ$  (22 June). Owing to the drift of the station, the time of the highest solar elevation varied. At the beginning the sun was highest at 0350 UTC, and at the end was highest at 1110 UTC (Figure 4d). In order to discuss the seasonality of spectral albedo and transmittance of snow and sea ice, we will focus on daily

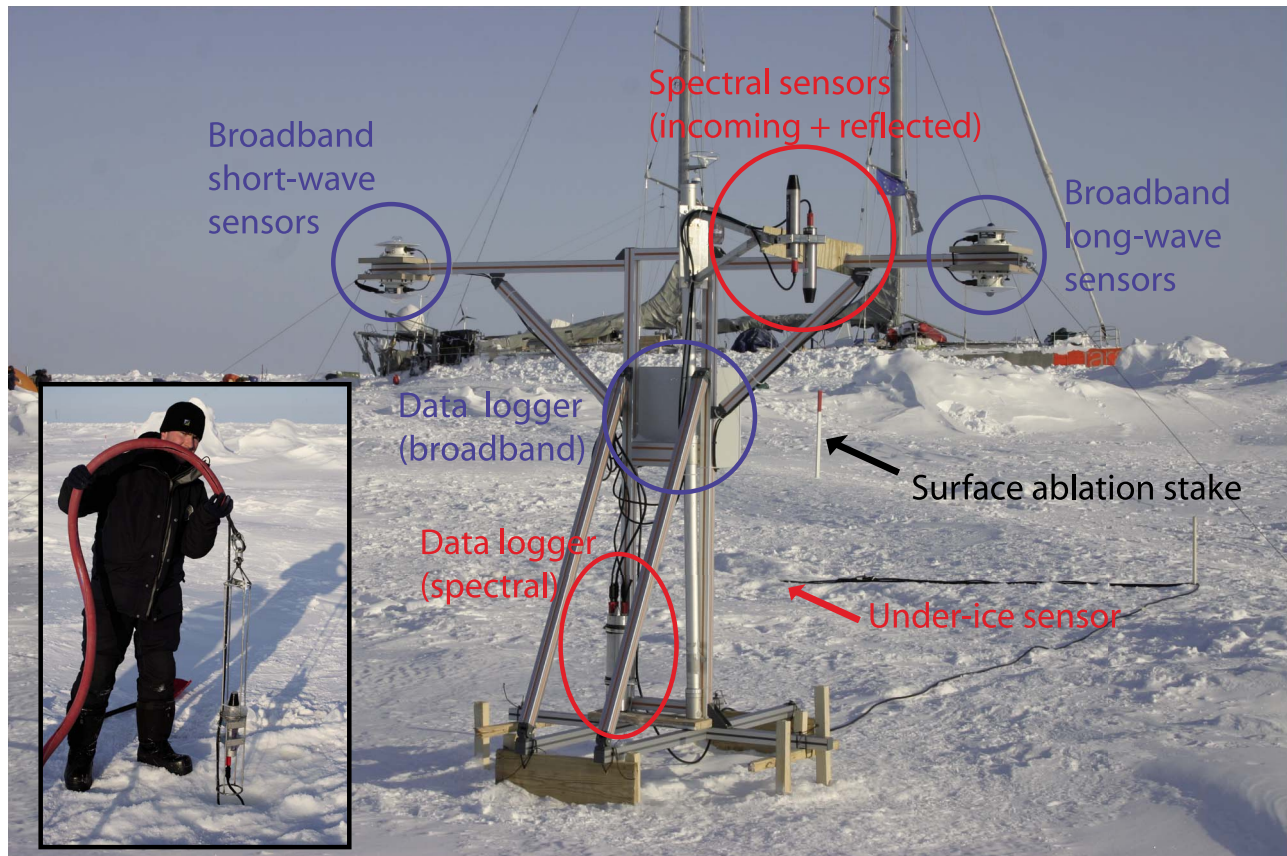


**Figure 2.** Photograph of setup (29 April 2007) showing both spectral and broadband irradiance sensors. The under-ice sensor is lowered at the end of the black cable behind the station and cannot be seen from the surface. The schooner *Tara* and the field camp can be seen in the background of the picture, but do not shadow the station at any time. The small inset picture shows the deployment of the under-ice sensor in its rack (photo: F. Latreille). Data cable and rope are protected through a red rubber tube.

spectra at times of highest solar elevation, and present these data only. On doing so, all presented data were recorded with solar elevation over  $10^\circ$  and similar solar azimuth angles of  $\sim 180^\circ$  (south). We consider this subset of data to be the most suitable and of the highest quality for studying seasonal changes. Owing to the drift of *Tara*, comparing data from the same UTC time of the day would also have included data with much lower incidence angles and from different directions. Nevertheless, recording a high temporal resolution data set was necessary to enable capturing data at the drifting local noon and to calculate daily mean values. Furthermore, the entire data set was used for quality checks and corrections during data processing.

[14] All data were calibrated to absolute spectra (in  $\text{mW m}^{-2} \text{nm}^{-1}$ ), and interpolated to a 1 nm grid before calculating ratios of spectra from different sensors (albedo and transmittance), to account for sensor-dependent wavelength grids. For the details on the data processing procedure, see *Nicolaus et al.* [2010]. Spectral albedo  $\alpha(\lambda, t)$  and spectral transmittance  $\tau(\lambda, t)$  were calculated as functions of wavelength  $\lambda$  and time  $t$  as described in *Nicolaus et al.* [2010]. Formulas for total (wavelength-integrated, from 350 to 920 nm) fluxes, albedo  $\alpha_T$ , and transmittance  $\tau_T$  as well as their temporal mean are also given by *Nicolaus et al.* [2010]. Note that our “total” quantities cover a limited

wavelength range, which is less than the real broadband measurements and quantities. It should be noted that all aspects related to transmitted irradiance and transmittance do not exclusively refer to optical properties of snow and ice, but also include the effect of the uppermost 1.4 m of water, where the under-ice sensor was installed and to where all spectra are corrected. Net fluxes into the ice ( $F_{\text{ICE}}(\lambda, t)$ ) and net absorption by snow and ice ( $F_{\text{ABS}}(\lambda, t)$ ) are calculated as

$$F_{\text{ICE}}(\lambda, t) = F_I(\lambda, t) - F_R(\lambda, t) \quad \text{and} \quad (1)$$

$$F_{\text{ABS}}(\lambda, t) = F_{\text{ICE}}(\lambda, t) - F_T(\lambda, t). \quad (2)$$

### 2.3. Broadband Irradiance Measurements

[15] The broadband short- and long-wave radiation setup (Figure 2) consisted of two Eppley precision spectral pyranometers for short-wave ( $S_{\text{up}}$  and  $S_{\text{down}}$ ) and two Eppley precision infrared radiometers, pyrgeometers, for long-wave irradiance ( $L_{\text{up}}$  and  $L_{\text{down}}$ ) measurements (see *Vihma et al.* [2008]). The short-wave radiometers cover a wavelength range from 280 to 2800 nm. In contrast to the spectral radiometers, the pyrgeometers and pyranometers had to be

cleaned daily, because snow, ice, and rime of variable amount covered the domes of the sensors.

[16] Surface temperature ( $T_{\text{surf}}$ ) is calculated from  $L_{\text{up}}$  and  $L_{\text{down}}$  as

$$T_{\text{surf}} = \sqrt[4]{\frac{L_{\text{up}} - (1 - \varepsilon) * L_{\text{down}}}{\varepsilon \sigma}} - 273.15, \quad (3)$$

using a surface emissivity  $\varepsilon = 0.98$  and Stefan-Boltzmann constant  $\sigma = 5.67 \times 10^{-8} \text{ W m}^{-2} \text{ K}^{-4}$ . The broadband albedo time series published by *Vihma et al.* [2008] is presented here, in order to compare it with the total albedo derived from spectral measurements.

#### 2.4. Measurements From an IMB

[17] For continuous measurements of sea ice and snow mass balance, an ice mass balance buoy (number 2007C) [*Perovich et al.*, 2008; *Richter-Menge et al.*, 2006] was installed approximately 250 m from the radiation station and did not drift more than 8 km away from the station during the observation period. The buoy was equipped with two acoustic sounders (one above the surface and one under the ice), a thermistor chain through the snow and sea ice, an air temperature sensor, a barometer, a GPS receiver, and a data acquisition and satellite communication unit. A complete set of measurements was made every 2 h from 0000 UTC 1 May to 1000 UTC 13 December 2007; we present data only until the end of spectral irradiance measurements. Here we focus on accumulation and ablation measurements of snow and sea ice. We define the snow-ice interface as  $z = 0$  of the vertical scale with positive values upward and negative values downward.

#### 2.5. Physical Snow and Sea-Ice Properties

[18] Snow thickness was obtained from snow stake readings and snow pits. Both observations were performed weekly by the *Tara* crew during the entire observation period of the radiometers. The snow stake profile consisted of nine stakes with 10 m spacing. Unfortunately, the initial reading of the snow-ice interface position and therefore the absolute snow thickness got lost. Hence, only relative changes, representing surface ablation, can be presented here. Stake 2 was closest to the radiation station (about 10 m away) and is discussed here. Snow pits were performed weekly at a designated site with snow and ice properties similar to those at the radiation station. Here we discuss only the surface observations of grain size and temperature, which we assume to be representative of a larger area, including directly below the radiation station. Snow grain size, defined here as the diameter of single crystals, was estimated with millimeter-grid sheets and a magnifying glass. The presence of snow was reported from snow pit observations during the entire summer, but after 21 June the surface actually consisted of deteriorated sea ice and all snow was gone. Snow grain sizes and snow thicknesses are therefore biased by unrealistically high values. We did not remove these observations as the deteriorated layer interacts with radiation like large-grained snow, not like crystalline ice.

[19] One ice core was drilled at the under-ice radiation site during the deployment of the sensor on 25 April 2007. Sea-

ice temperature was measured using a handheld PT100 thermometer (accuracy  $\pm 0.1^\circ\text{C}$ ). Afterward, the core was sealed and shipped frozen to a freezer lab for further analysis. Vertical thin sections of the entire core were prepared and photographed with and without crossed polarizers, allowing for texture analysis and classification (columnar, granular, mixed). On the basis of the texture result, the ice core was cut into 28 segments of irregular thickness, 4.5–10.5 cm, which were melted and used for salinity and  $\delta^{18}\text{O}$  measurements. Compared to using a regular cutting scheme, this structure-based segmenting procedure eases combined analysis of all parameters.

### 3. Results

#### 3.1. General Surface Properties and Meteorological Conditions

[20] Photos of the surroundings of the station (Figure 3) illustrate the seasonality of surface conditions for selected dates between 18 May and 28 August. The seasonal evolution of surface properties shows five distinct phases, similar to those defined by *Perovich et al.* [2002a]. These phases and selected characteristic events of meteorological, snow, and sea-ice conditions during the drift of *Tara* are summarized in Table 1.

##### *Phase I: Dry snow (29 April to 9 June)*

[21] The observations started under typical spring conditions of Arctic sea ice. Snow covered most of the sea-ice surface, as shown on the photo from 18 May (Figure 3a), and the surface was dry and cold with temperatures significantly below freezing until the second week of June (Figure 4a). The snow was packed and redistributed by wind and had experienced some metamorphosis and compaction. *Vihma et al.* [2008] reported the first above-freezing air temperatures on 8 June, and the IMB reported the snow surface temperature reached  $0^\circ\text{C}$  for the first time on 12 June (Figure 4a). During phase I, snow pits show all temperatures within the snow were still below freezing. Surface snow grain size estimates varied between 1 and 4 mm before melt onset (Figure 4a), but these observations most likely overestimate single crystal sizes.

##### *Phase II: Melting snow (10–21 June)*

[22] After melt onset on 10 June (defined from spectral albedo data; see section 3.4), snow thickness decreased until the snow cover vanished completely on 21 June (Figures 4b and 4c), when the first melt ponds were also observed [*Sankelo et al.*, 2010]. Surface temperatures remained at the melting point of  $0^\circ\text{C}$  from 20 June to the end of the melting season (Figure 4a). Sea-ice temperatures also increased significantly during phase II, and as the ice got warmer than  $-4^\circ\text{C}$ , ice cores showed that the salinity of the sea ice decreased rapidly. The largest changes were observed at the ice surface and the main desalination event was observed between 5 and 19 June (ice core data not shown here).

##### *Phase III: Water-saturated surface (22 June to 2 July)*

[23] After all the snow was gone, surface ablation continued (Figures 4b and 4c) and led to an entirely water-saturated sea-ice surface (Figures 3b and 3c), with meltwater standing on the ice without draining. Also, the formation of the first discrete melt ponds within this water-saturated surface was observed. Melt-pond coverage increased from 3% to 14% between 24 and 30 June and continued increasing into

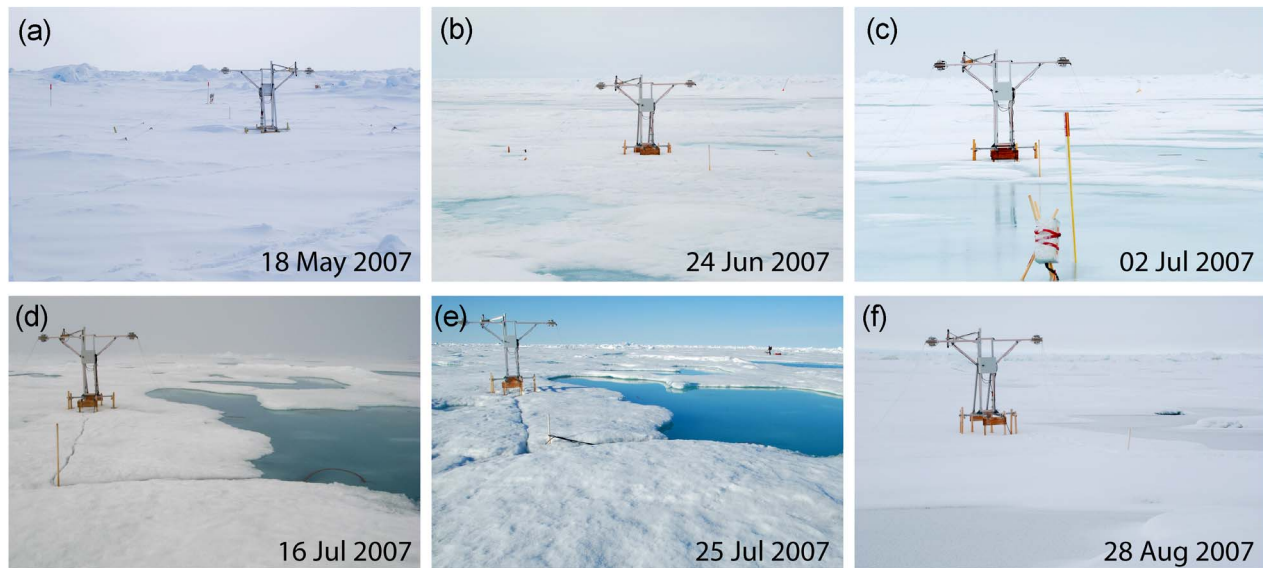


**Figure 3.** Seasonal changes of surface conditions around the radiation station. Photographs show (a) late spring condition (18 May), (b) early melt-pond formation (24 June), (c) completely water saturated surface (2 July), (d, e) further melt-pond evolution (16 and 25 July), and (f) autumn freezeup (28 August). Note that the photo from 18 May was taken from the opposite side compared to all others. All photos were taken by crew members of *Tara* (mostly by T. Palo, all © *Tara Expeditions*) and postprocessed by the authors.

**Table 1.** Time Line and Characteristic Events of the *Tara* Drift During the Presented Observation Period of Spectral Irradiance Measurements (29 Apr to 5 Sep 2007)<sup>a</sup>

Date in 2007 (Duration)	Event/Description	Data Set
<i>Phase I: Dry snow</i>		
29 Apr to 09 Jun (42 days)		
08 Jun	Air temperature exceeds 0°C	Weather station
09 Jun	Total albedo maximum	Radiation
12 Jun	Surface temperature reaches 0°C	IMB
<i>Phase II: Melting snow</i>		
10–21 Jun (12 days)		
10 Jun	Melt onset (drop of albedo in near infrared)	Radiation
12 Jun	Snow surface temperature reaches 0°C	IMB
20 Jun	Surface temperature constant at melting point	IMB
21 Jun	All snow is gone, surface ablation continues; first melt ponds	IMB photos
<i>Phase III: Water-saturated surface</i>		
22 Jun to 2 Jul (11 days)		
22 Jun	Start of shift in max. transmittance wavelength	Radiation
01 Jul	Total transmittance maximum (0.066)	Radiation
02 Jul	Total albedo minimum (0.66)	Radiation
	Most surface area is water-saturated	Photos
<i>Phase IV: Scattering surface</i>		
3 Jul to 14 Aug (43 days)		
3 to 14 Jul (12 days)	Phase IVa: Surface drainage	
Between 4 and 6 Jul	Drainage of sea-ice surface	Photos
15 Jul to 14 Aug (31 days)	Phase IVb: Increased biological absorption	
Between 16 Jul and 09 Aug	Sea-ice bottom growth turns into bottom ablation	IMB
14 Aug	Total albedo minimum (0.65)	Radiation
	First new snow after summer	IMB
<i>Phase V: Autumn freezeup</i>		
15 Aug to 05 Sep (21 days)		
15 Aug	Start of freezeup (albedo increase)	Radiation
28 Aug	Retrieval of under-ice sensor	

<sup>a</sup>Table 1 is structured into five phases, describing the seasonality of snow and sea-ice properties. Phase names are according to *Perovich et al. [2002b]*, when applicable. Some events are highlighted in the map in Figure 1. The events are primarily identified by the data set given in the last column, but using other observations gives similar results.

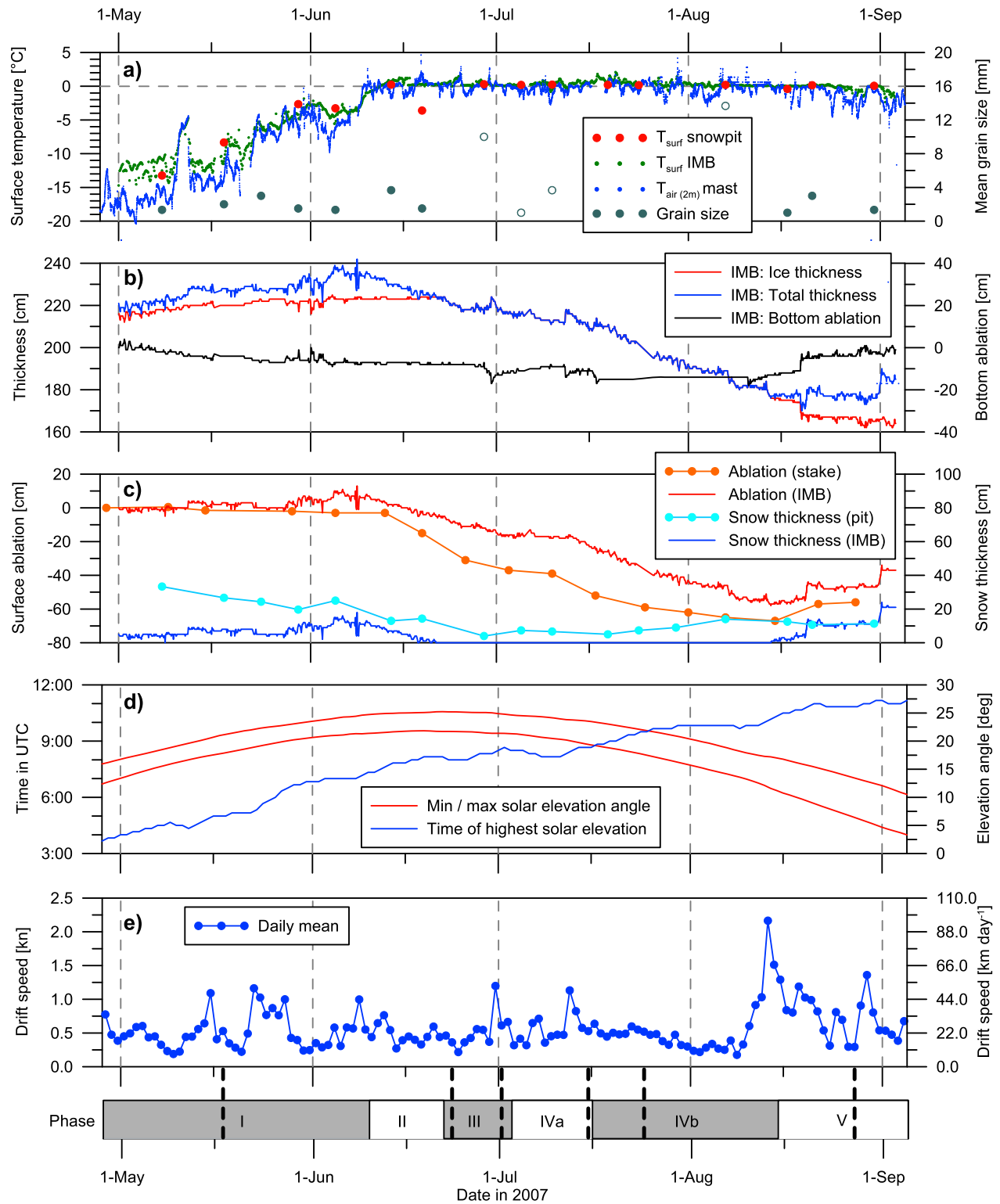


**Figure 4.** (a) Surface temperatures from snow pits and IMB, and 2 m air temperature from mast measurements (replotted from [Vihma et al., 2008]), as well as snow grain size. Observations of grain sizes during times when no snow cover was present are shown as open symbols. (b) Sea-ice and total (snow + ice) thickness as well as bottom ablation from IMB measurements. (c) Snow ablation and thickness from IMB and manual observations. (d) Time of highest solar elevation angle and minimum and maximum solar elevation angles. (e) Drift speed of *Tara* based on GPS positions. All data are based on the measurements as presented in Figure 6 and are plotted at noon of the day (1200 UTC). Minor ticks on the time axis are on 16th of each month. The phases described in the text and Table 1 are given on the bottom and as grid lines in each plate. Thick dashed vertical lines at the bottom indicate dates of photos in Figure 3.

phase IV [see also *Sankelo et al.*, 2010]. During this phase, a melt pond formed close to the radiation station.

*Phase IV: Scattering surface (3 July to 14 August)*

[24] The surface drained from 4 to 6 July, resulting in distinct melt ponds and drained areas of deteriorated sea ice, forming a surface scattering layer. These surface conditions are shown in the photographs from 16 and 25 July (Figures 3d and 3e). The melt-pond fraction was 15% on 21 July, the last day of quantified melt-pond observations [*Sankelo et al.*, 2010]. Afterward, surface ablation continued (Figures 4b and 4c) and the melt-pond fraction increased to a maximum of 30%–40%, estimated from photographs taken from different positions at irregular intervals. Otherwise, surface properties of the melting and deteriorating sea ice did not change remarkably, and temperatures remained at the melting point (Figure 4a) until autumn freezeup.

*Phase V: Autumn freezeup (15 August to 5 September)*

[25] After 14 August, air and surface temperatures below 0°C resulted in surface freezing and snow accumulation. The photograph from 28 August (Figure 3f) shows the surface after freezeup, when former melt ponds are still clearly visible through the new snow.

*Weather and drift*

[26] Cloud coverage was highly variable until mid-May and mostly overcast afterward. A longer period of almost clear sky was observed from 17 to 21 June. Occasionally snow or rain was observed, with two prominent snowfall events during the melt season, on 27 June and 6 July. The first snowfall after freezeup started on 14 August.

[27] Analysis of IMB position data (recorded every 2 hours) resulted in a mean drift velocity of *Tara* of 0.56 kn (24.9 km day<sup>-1</sup>) during the observation period (Figures 4e and 1, and *Vihma et al.* [2008]). Most prominent was a peak in drift velocity from 8 to 13 August, resulting in a maximum speed of 2.2 kn (97.8 km day<sup>-1</sup>).

### 3.2. Snow and Sea-Ice Thickness

[28] Ice thickness at the IMB site increased from 2.14 m (1 May) to a maximum of 2.25 m (4 June). This thickness increase was due to bottom ice growth (Figure 4b). Afterward, ice thickness decreased to its minimum of 1.62 m at the end of observation period. In total, summer ice thickness decreased by 0.63 m, with 0.53 m of surface ablation and 0.10 m of bottom melt. Even though total ice thickness decreased after 4 June, basal ice growth continued until sometime between 16 July and 9 August, after which the ice bottom began to ablate. Because of imprecise readings of the under-ice sonic of the IMB, this timing cannot be determined precisely. Since 10 August, bottom ablation continued until the end of the observation period (Figure 4b) and also beyond this until mid-October (data not shown here). Snow thickness from the IMB was initially 0.05 m, increased to 0.18 m (8 June), and then decreased, reaching zero on 21 June. From the first new snow on 14 August to the end of the observation period, snow accumulated to a thickness of 0.24 m.

[29] Snow stake and IMB measurements show very similar surface ablation over the entire season (13 June to 17 August), despite being observed at different sites. It amounted to 0.64 m at the snow stake, which was closest to the radiation station, but there was up to 0.2 m more net ablation at the

stake than at the IMB during July, including the effect that stake readings do not show accumulation before melt onset (Figure 4c).

[30] Comparing initial snow and sea-ice thicknesses at the radiation station, sea ice was initially 0.14 m thicker and snow was 0.05 m thinner at the IMB site than at the radiation station. Here the time series measurements at the IMB are used to discuss the optical data, because no thickness measurements were performed directly at the radiation station. Considering the generally high lateral variability of snow and sea-ice properties on a floe-scale, both stations represent the same snow and ice regimes. A combined analysis of both data sets seems reasonable.

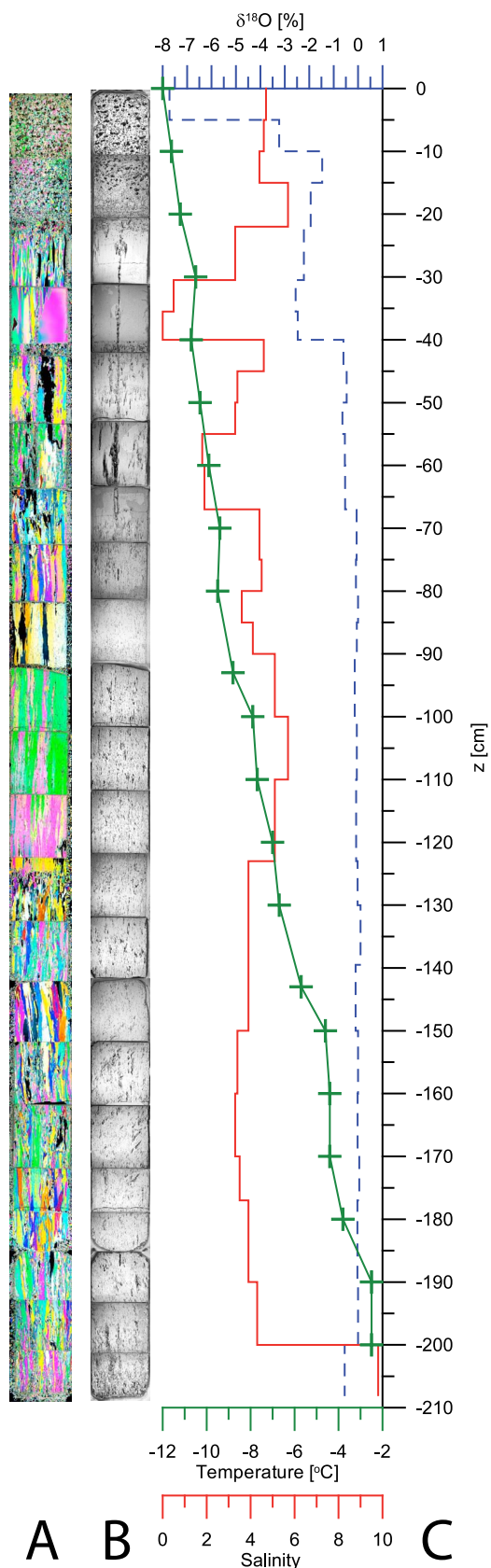
### 3.3. Sea-Ice Texture

[31] A photo mosaic of sea-ice texture from the core (25 April 2007) at the under-ice sensor site is shown in Figure 5. Ice thickness, freeboard and snow thickness were 2.06, 0.10 and 0.08 m, respectively. Core length (four segments) was measured to be 2.08 m. The topmost 0.22 m of fine-grained granular ice was most likely due to snow-ice formation during the previous autumn/winter, indicating that surface flooding would have occurred. This snow-ice formation can also be seen from negative  $\delta^{18}\text{O}$  values with a minimum of  $-7.7$  (topmost 5 cm). Between 0.22 and 0.40 m, the ice was very transparent, pointing to a former summer surface. The amorph crystals, low salinities (0.0 between 0.35 and 0.40 m), and negative  $\delta^{18}\text{O}$  are indications of a refrozen melt pond between 0.3 and 0.4 m.

[32] A sharp interface and a thin, 2 cm layer of granular ice marks the top of the next section, extending down to the next interface at 0.67 m. This section is dominated by columnar ice with large brine channels. This might result from the previous (2006) summer season. As the photos under plain light show (Figure 5b), these brine channel structures end at 0.67 m and are not present anywhere deeper in the core. Also, salinity increases to values of 3.5 and above for the rest of the core. Hence, we assume that this (at 0.67 m) was the former summer underside, resulting in an ice thickness of  $\sim 0.45$  m (0.22–0.67 m) at the end of the last ablation season.

[33] Further down, columnar crystals dominate the ice texture and  $\delta^{18}\text{O}$  values are near zero, indicating bottom ice growth under calm conditions. The section to 1.23 m stands out for very large ( $>10$  cm long) crystals and the ice contains a lot of small and unstructured inclusions (brine pockets and air bubbles). At 1.23 m, a distinct transition from large columnar to small granular crystals can be seen (Figure 5a), while salinity and  $\delta^{18}\text{O}$  profiles do not reveal striking changes. This hints at a frazil ice or rafting event. Another, similar, interface within the columnar ice occurs at 1.77 m.

[34] In total, 88% of the ice crystals were columnar, 10% granular and 2% mixed crystals. Initial sea-ice temperature increased almost linearly from  $-12.0^\circ\text{C}$  at the surface to  $-2.5^\circ\text{C}$  at the ice-ocean interface and mean salinity was 4.1 (Figure 5c). Mean value of  $\delta^{18}\text{O}$  was  $-0.7$ , with means of  $-3.0$  for the snow ice and refrozen melt pond (0–0.22 m),  $-0.6$  for the old sea ice (0.22–0.67 m), and  $-0.1$  for the mostly columnar sea ice below 0.67 m.



### 3.4. Spectral Irradiance, Albedo, and Transmittance

[35] Figure 6 shows time series of spectral irradiances (incident, reflected, transmitted), spectral albedo, and spectral transmittance, plotted daily at solar noon. Corresponding time series of total (350–920 nm) quantities are plotted in Figure 7, also highlighting the different phases described above. Statistical quantities are summarized in Tables 2 and 3. The presented once-daily spectra are, as discussed above, considered to have the highest quality and to be the most representative for discussions of seasonal changes. As a consequence, sub-diurnal variations and short weather events are not resolved in the presented data. Here we present the results of the radiation measurements between 29 April and 4 September, separated into the above-mentioned five phases. The first and the last phase extend beyond the observation period.

#### Phase I: Dry snow (29 April to 9 June)

[36] During the first phase, the total incident irradiance ranged between  $139$  and  $315 \text{ W m}^{-2}$  with a mean of  $205 \text{ W m}^{-2}$  and a standard deviation of  $38 \text{ W m}^{-2}$  (i.e.,  $205 \pm 38 \text{ W m}^{-2}$ ). During the entire observation period, irradiance was highly variable, a result of changing cloud conditions. The seasonal cycle of solar irradiance resulted in highest incident radiation ( $315 \text{ W m}^{-2}$ , 8 June) at the end of phase I with continued high values during phase II (Figure 7b). Albedo was above 0.75 for all wavelengths, with maxima around 0.90 between 400 and 700 nm (Figures 6d and 8a). On account of new snow accumulation and snow drift, albedo values increased with time to a total maximum of 0.93 on 9 June. On average,  $22.3 \text{ W m}^{-2}$  was absorbed by the snow and sea ice during phase I. Transmitted irradiance was below  $3.0 \text{ mW m}^{-2} \text{ nm}^{-1}$  for all wavelengths before 9 June (Figure 6c) and mean total transmitted irradiance and total transmittance were  $0.34 \text{ W m}^{-2}$  and 0.002, respectively (Figures 7a and 7c).

#### Phase II: Melting snow (10–21 June)

[37] Mean total irradiance was highest during phase II ( $277 \pm 40 \text{ W m}^{-2}$ ) with maximum values around  $760 \text{ mW m}^{-2} \text{ nm}^{-1}$  (at 460 nm) during clear-sky phases on 14 and 17–21 June, just before the summer solstice. The main characteristics of this phase were melt onset (10 June) and subsequent snowmelt, which became most obvious in the spectral albedo measurements. After its maximum on 9 June, total albedo decreased steadily during phase II, with the most significant decrease in near-infrared albedo. While albedo values at shorter wavelengths decreased only moderately, a strong and rapid decrease of near-infrared values, by 0.12 from 0.84 to 0.72, was observed between 9 and 11 June (Figure 6d), almost doubling the energy absorption at long wavelengths. This change and the increasing liquid water content in snow stands out in the ratio of albedo at 900 nm to albedo at 500 nm ( $\alpha(900)/\alpha(500)$ ), which decreased by 19% between 6 and 12 June (Figure 7d). Coincident with melt onset, the amount of total transmitted light increased over 12 days by a factor of 10, to a mean of  $2.2 \text{ W m}^{-2}$  and a

**Figure 5.** Photo mosaic of thin sections (a) photographed with crossed polarizers and (b) photographed with transmitted light, and (c) temperature, salinity, and  $\delta^{18}\text{O}$  profiles from an ice core, retrieved from the under-ice sensor site on 25 April 2007. Total core length was 2.08 m and the snow-ice interface was at  $z = 0$ .

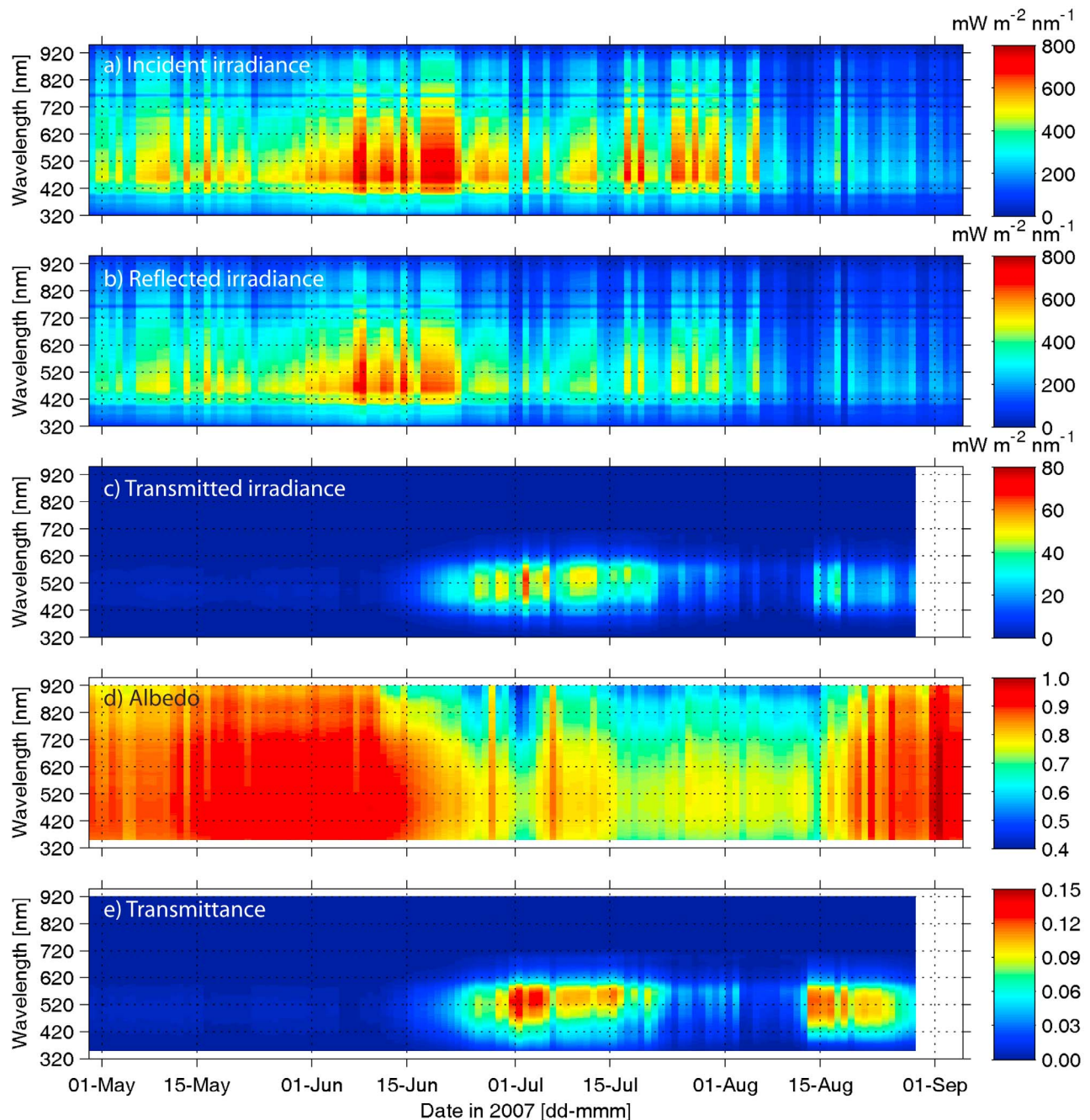


**Figure 6.** Time series of (a) incoming, (b) reflected, and (c) transmitted spectral irradiance as well as spectral (d) albedo and (e) transmittance. One spectrum is shown per day, from the observation with the highest solar elevation angle. As the under-ice sensor had to be retrieved on 28 August, no transmitted irradiance or transmittance data are available afterward. Blanked (white) areas in the albedo and transmittance data result from the reduction in wavelength range due to data quality issues.

maximum value of  $5.5 \text{ W m}^{-2}$ . Figure 7c shows this first significant increase after a long period of low-light conditions under the ice. This first increase did not affect the wavelength of maximum transmitted irradiance, which remained almost constant around 500 nm (Figure 7d). In contrast, the ratio of transmittance at 600 to transmittance at 450 nm ( $\tau(600)/\tau(450)$ ) started to increase slightly. This ratio is a sensitive indicator of biomass [Perovich *et al.*, 1993].

#### Phase III: Water-saturated surface (22 June to 2 July)

[38] Phase III is characterized by the highest total flux into the ice (mean:  $55 \text{ W m}^{-2}$ , max. on 2 July:  $85 \text{ W m}^{-2}$ ) and highest total net absorption by the ice (mean:  $47 \text{ W m}^{-2}$ , max. on 2 July:  $73 \text{ W m}^{-2}$ ) during the observation period (Figures 7c and 9). Also, the decrease of albedo and increase of transmittance continued in phase III, even though the surface was already snow-free at the beginning of this phase

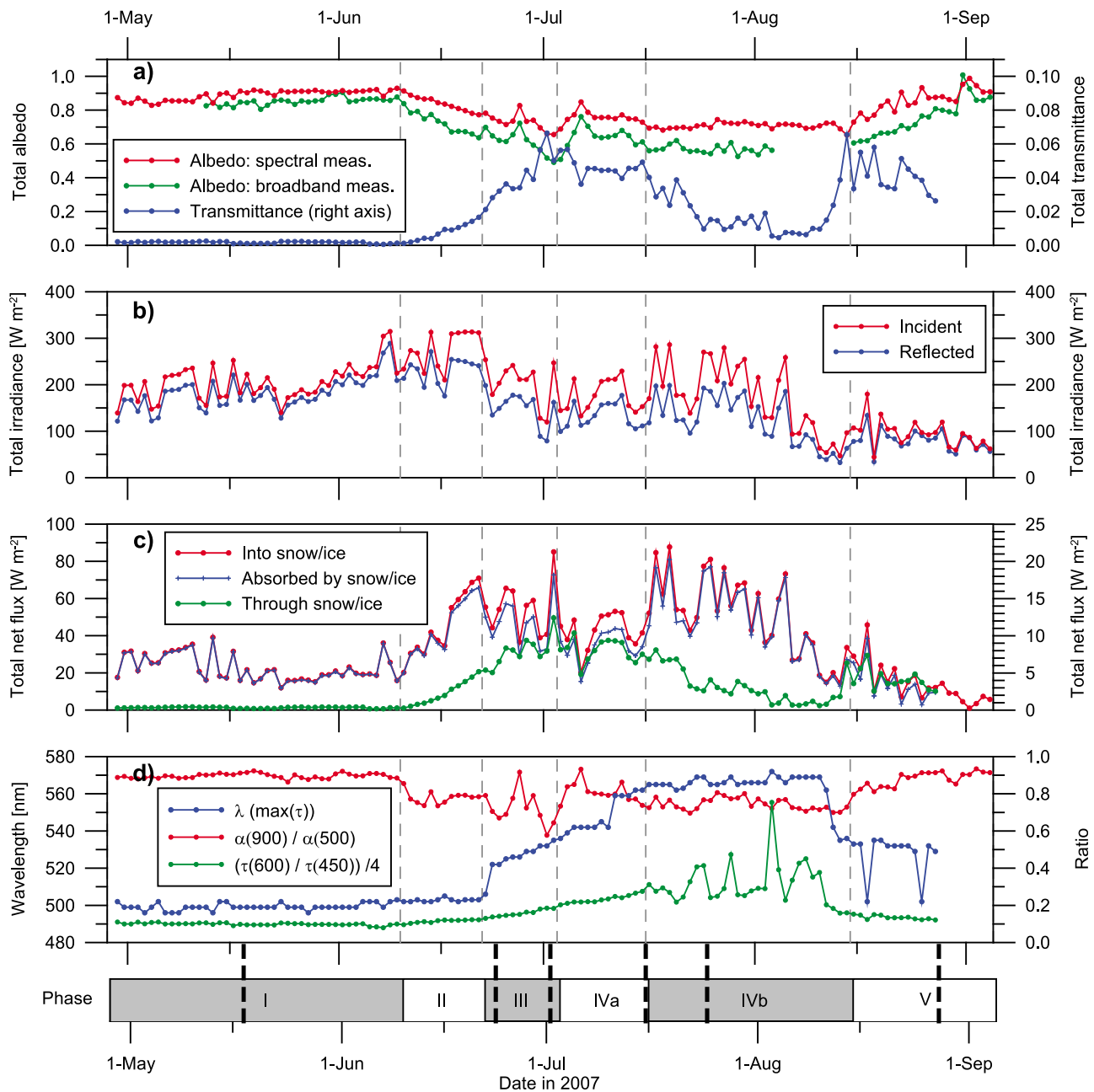


**Figure 7.** (a) Total (350–920 nm) albedo and transmittance from spectral measurements and broadband (280–2800 nm) albedo from broadband measurements (replotted from *Vihma et al.* [2008]). (b) Total incident and reflected irradiance. (c) Total net fluxes into snow and sea ice, absorbed in snow and sea ice (both referring to left y axis), and transmitted through snow and sea ice (referring to right y axis; note different scale). (d) Wavelength ( $\lambda$ ) of maximum transmittance and ratios of spectral albedo ( $\alpha$ ) and transmittance ( $\tau$ ) at selected wavelengths. The transmittance ratio was divided by 4 for easier presentation. All data are based on the measurements presented in Figure 6 and are plotted at noon of the day (1200 UTC). Minor ticks on the time axis are on 16th of each month. The phases described in the text and Table 1 are given at the bottom and as grid lines in each plate. Thick dashed vertical lines at the bottom indicate dates of photos in Figure 3.

(since 21 June). These maximum values of flux into and through the ice were observed despite the fact that the mean incident irradiance ( $205 \pm 45 \text{ W m}^{-2}$ ) was approximately 25% lower than during its maximum in phase II, indicating significant changes in the vertical partitioning of solar irradiance.

[39] Total albedo decreased to a mean of 0.73 (from 0.89 during phase I), with strong reductions at all wavelengths, and reached the phase III minimum of 0.66 on 2 July (the overall minimum was 0.65 on 14 August). At this time, spectral albedo maxima (around 500 nm) were around 0.73, and near-infrared minima were between 0.4 and 0.5

**Table 2.** Statistics About Total (320–950 nm) and PAR (400–700 nm) Fluxes, Albedo, and Transmittance From Spectral Radiometers During 29 Apr–27 Aug 2007 (121 Days), the Time When All Three Radiometers Were Installed<sup>a</sup>

	Minimum		Maximum		Mean	SD	Sum (MJ m <sup>-2</sup> )
Incident (total, W m <sup>-2</sup> )	44.3	(18 Aug)	314.7	(08 Jun)	190	64	1768
Incident (PAR, W m <sup>-2</sup> )	30.1	(18 Aug)	202.6	(08 Jun)	122	40	1129
Reflected (total, W m <sup>-2</sup> )	32.5	(13 Aug)	289.1	(08 Jun)	154	56	1453
Reflected (PAR, W m <sup>-2</sup> )	23.2	(13 Aug)	189.4	(08 Jun)	101	35	953
Transmitted (total, W m <sup>-2</sup> )	0.18	(07 Jun)	12.41	(02 Jul)	3.1	3.1	30
Transmitted (PAR, W m <sup>-2</sup> )	0.18	(07 Jun)	11.67	(02 Jul)	3.0	2.9	29
Albedo (total)	0.65	(14 Aug)	0.93	(25 Aug)	0.81	0.08	
Albedo (PAR)	0.68	(14 Aug)	0.95	(25 Aug)	0.83	0.08	
Transmittance (total)	0.001	(07 Jun)	0.066	(01 Jul)	0.017	0.019	
Transmittance (PAR)	0.001	(07 Jun)	0.097	(01 Jul)	0.025	0.028	
Net surface flux (total, W m <sup>-2</sup> )	6.5	(25 Aug)	87.7	(19 Jul)	36	20	314
Net absorption in snow and ice (total, W m <sup>-2</sup> )	2.8	(25 Aug)	80.9	(19 Jul)	33	18	283

<sup>a</sup>Table 2 contains minimum, maximum, mean, and 1 standard deviation values as well as the sum over the period. All values are based on the presented data set at times of highest solar elevation angles, except the total energy, which is calculated from the full (30 min resolution) data. PAR, photosynthetically active radiation.

(Figure 8a). Mean total transmittance of the sea ice increased from 0.002 (phase I) to 0.038 and reached its maximum during this phase, 0.066, on 1 July. As a consequence, total transmitted irradiance into the upper ocean (mean: 7.9 W m<sup>-2</sup>, maximum on 2 July: 12.4 W m<sup>-2</sup>) was near the highest values observed, but slightly lower than during the next phase. Spectral transmittance maxima of 0.13 were measured for wavelengths between 530 and 535 nm (Figure 8b, 2 July), showing that the wavelength of maximum transmitted irradiance increased significantly after 22 June (Figure 7d), when all the snow was gone and meltwater ponded on the surface. The highest fluxes of 66 mW m<sup>-2</sup> nm<sup>-1</sup> were measured at a wavelength of 532 nm, while hardly any energy was transmitted at wavelengths above 720 nm. The decrease of albedo and increase of transmittance were interrupted only by a new snow event on 27 June, when fine-grained, dry snow increased surface reflectivity temporarily. This event is evident in several time series in Figures 6 and 7. Mean transmitted photosynthetically active radiation (PAR, 400–700 nm) was 7.4 W m<sup>-2</sup>, equivalent to 94% of the total transmitted spectrum and 5.6% of the surface PAR irradiance.

[40] Melt ponds started to form during this phase, and one melt pond was close to the radiation station (Figure 3), so the measurements describe a mixture of the bare summer sea-ice surface and the melt pond, but the mixture is not representative of the area fraction of melt ponds on the floe. The pond's effect on the measured fluxes of  $F_R$  and  $F_T$  varied over time as the pond developed. It was small during most of this phase, when the entire surface was water-saturated; the pond started to stand out only at the end. However, the melt pond is influential as it has different optical properties, resulting in lower albedo and higher transmittance observations compared to bare sea ice.

#### Phase IV: Scattering surface (3 July to 14 August)

[41] Unlike the results of the snow and sea-ice observations, the radiation observations show two distinct phases during phase IV. Hence, those are discussed as phase IVa until 14 July and phase IVb afterward.

[42] The effect of the nearby melt pond was most significant during phase IV, but different for  $F_R$  and  $F_T$  measurements. During its maximum extent, the melt pond was more than 3 m away from the point below the  $F_R$  sensor, while the  $F_T$  sensor was right below the pond edge. At this time of maximum influence, the pond surface covered about

**Table 3.** Mean Total (320–950 nm) and PAR (400–700 nm) Fluxes, Albedo, and Transmittance for Each of the Different Phases (I–V) Calculated From Measurements With the Spectral Radiometers, Along With Values from the Broadband Radiometers (280–2800 nm)<sup>a</sup>

Phase	I	II	III	IV	IVa	IVb	V
Incident (total, W m <sup>-2</sup> )	204.7	<b>277.0</b>	204.7	173.6	176.9	172.4	103.8
Incident (PAR, W m <sup>-2</sup> )	129.7	<b>176.2</b>	133.0	111.8	114.7	110.8	66.8
Reflected (total, W m <sup>-2</sup> )	182.1	<b>231.5</b>	150.2	125.6	134.5	122.1	85.3
Reflected (PAR, W m <sup>-2</sup> )	117.35	<b>152.7</b>	102.0	84.0	89.6	81.8	56.0
Transmitted (total, W m <sup>-2</sup> )	<i>0.34</i>	2.25	7.86	4.62	<b>8.09</b>	3.28	4.07
Transmitted (PAR, W m <sup>-2</sup> )	<i>0.33</i>	2.14	7.42	4.37	<b>7.60</b>	3.12	3.89
Albedo (total)	<b>0.89</b>	0.84	0.73	0.72	0.76	<i>0.71</i>	0.82
Albedo (PAR)	<b>0.90</b>	0.87	0.76	0.75	0.78	<i>0.74</i>	0.84
Transmittance (total)	<i>0.002</i>	0.008	0.038	0.027	<b>0.046</b>	0.019	0.039
Transmittance (PAR)	<i>0.003</i>	0.012	0.056	0.039	<b>0.066</b>	0.028	0.058
Net surface flux (total, W m <sup>-2</sup> )	22.6	45.5	<b>54.5</b>	48.1	42.4	50.2	18.5
Net absorption snow and ice (total, W m <sup>-2</sup> )	22.3	43.3	46.7	43.4	34.3	<b>47.0</b>	14.4
Broadband incident (W m <sup>-2</sup> )		358.6	268.0		234.0		132.8
Broadband reflected (W m <sup>-2</sup> )		235.3	140.8		141.9		65.4
Broadband albedo		0.72	0.62		0.64		0.66

<sup>a</sup>Description and times for each phase are given in Table 1. Broadband data are not available for all times during phases I and IVb [Vihma et al., 2008]; hence, no data are given for these phases. All data are based on the presented data set at times of highest solar elevation angles. Minima (italic) and maxima (bold) are highlighted, but not for the broadband measurements, because those are not available for all phases. PAR, photosynthetically active radiation.

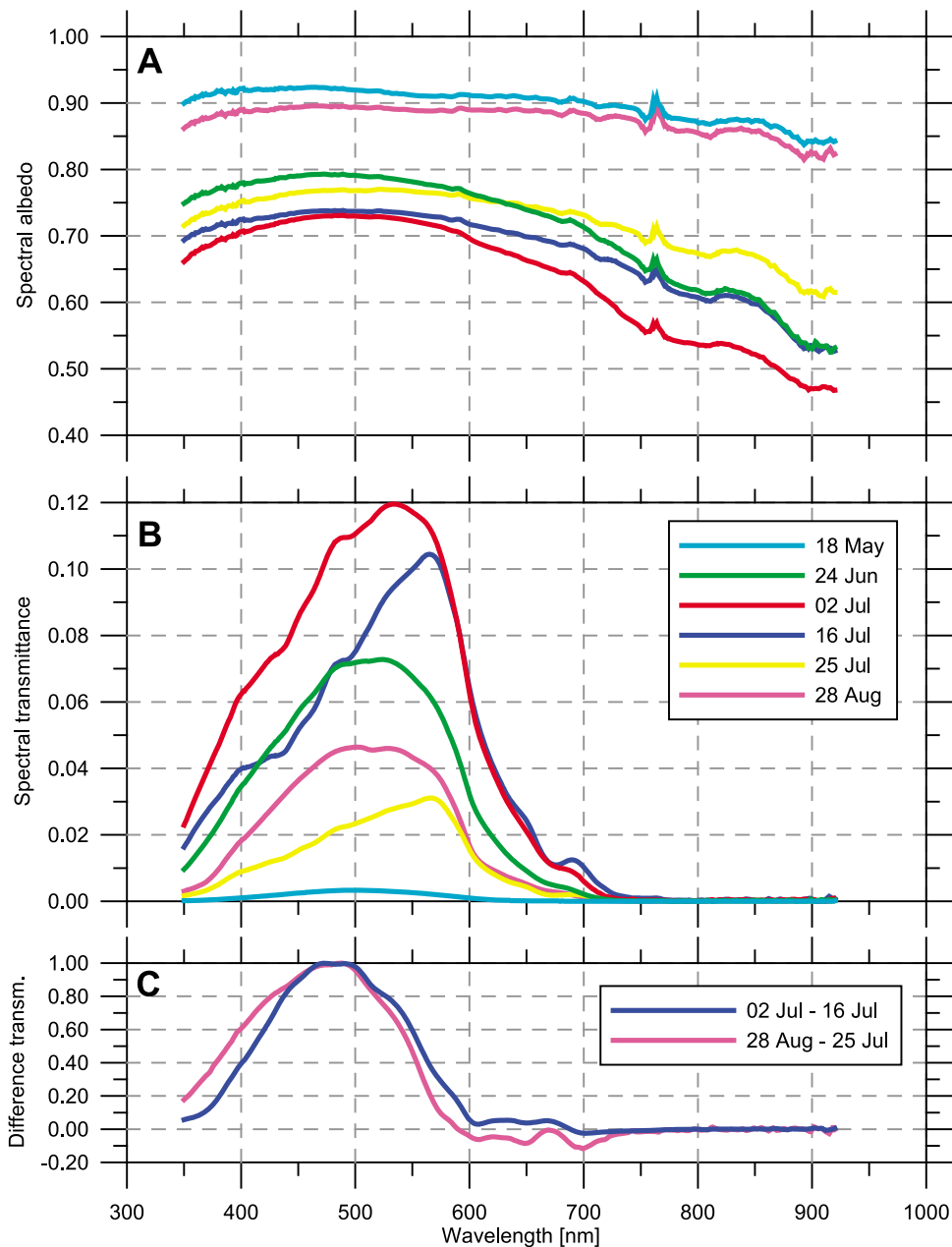


**Figure 8.** (a) Albedo and (b) transmittance spectra for different surface conditions, as shown in Figure 3. The legend in Figure 8b refers to both Figures 8a and 8b. (c) Normalized difference of transmittance spectra ( $\tau(\lambda, t_1) - \tau(\lambda, t_2)$ ).

one sixth of the field of view of the  $F_R$  sensor and half of the field of the  $F_T$  sensor. Accounting for the sensors' cosine-weighted response, we estimate a maximum representation of the melt pond of 5% in the albedo and 50% in the transmittance measurements. Therefore, while the albedo presented here is mostly representative of the bare portions of the floe during phase IV, the transmission is representative of a mix of the bare and ponded portions.

#### *Phase IVa: Surface drainage (3–14 July)*

[43] Phase IV (IVa) began on 3 July, after the summer maximum of transmittance. The first days (until 6 July) were characterized by increasing albedo (from 0.69 to 0.85) and

decreasing transmittance (from 0.056 to 0.036; Figures 6 and 7a). These changes were mainly related to the drainage of the sea-ice surface, resulting in bare sea ice with a surface scattering layer and distinct melt ponds. In addition, there was a little new snow observed. Afterward, until the end of phase IV (14 August), total albedo decreased slowly to its overall minimum of 0.65. During this time, the most significant change on the ice surface was the development of melt ponds. The shape of the albedo spectra did not show significant changes, and maxima ranged from 0.78 to 0.80 (470–520 nm, phase IVa) and were significantly higher than near infrared values (0.60–0.70). Owing to lower incident

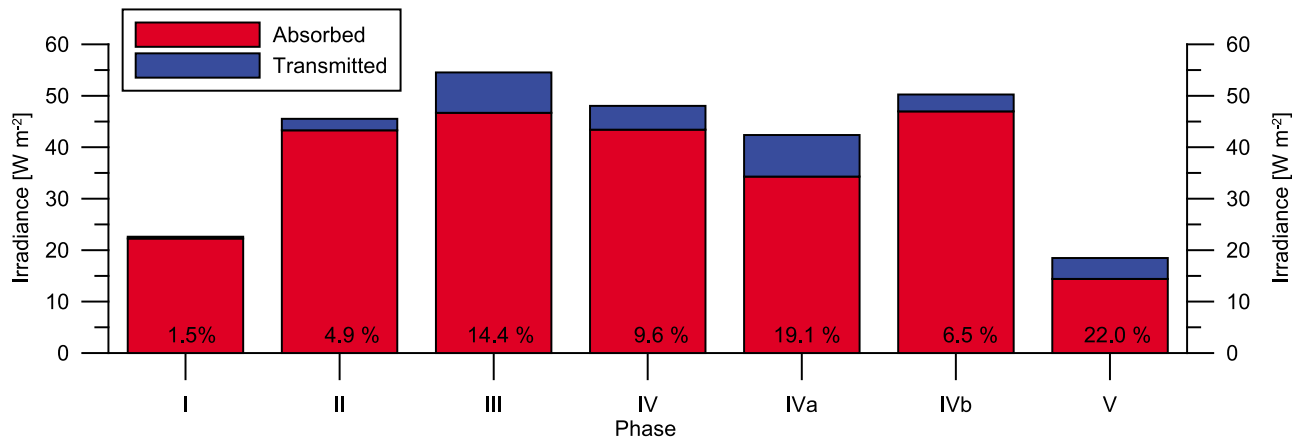


**Figure 9.** Net fluxes absorbed by snow and sea ice, and transmitted through snow and sea ice into the upper ocean for the different phases in Table 1. Flux values are listed in Table 2. The sum of both (=height of columns) is the net flux into snow, sea ice, and the water below. The numbers above the  $x$  axis give the fraction of the net flux into snow and sea ice that is transmitted to the under-ice sensor. The mean of this fraction over all phases is 8.6%.

fluxes (total mean:  $177 \text{ W m}^{-2}$ ), total net fluxes into the ice and total absorption within the ice were moderate, 42 and  $34 \text{ W m}^{-2}$  (Figure 7c), respectively, during the first half of July.

[44] In contrast to the albedo observations, the decrease in transmitted irradiance was accompanied by significant changes in the spectral shape of the transmittance. These changes are most obvious during phase IVa. Although the total transmittance did not change much (total mean:  $0.046 \pm 0.006$ ) during phase IVa, the wavelength of maximum transmittance increased from 536 (3 July) to 559 nm (14 July), including a major step from 10 to 11 July (Figure 7d). Furthermore, the  $\tau(600)/\tau(450)$  ratio continued its steady increase, pointing to increased absorption at wavelengths around 450 nm (Figure 7d). Comparing the spectra from 2 and 16 July (Figure 8b) illustrates the shift in wavelength of the transmittance maximum and the reduction in transmittance at wavelengths between 350 and 580 nm. Transmittance at wavelengths longer than 600 nm shows hardly any change (Figure 8c).

*Phase IVb: Increased biological absorption (14 July to 14 August)*

[45] As in phase IVa, spectral albedo during phase IVb varied little before mid-August, as it was controlled by the drained surface scattering layer (total mean:  $0.71 \pm 0.02$ ). After 4 August, incident irradiance was significantly lower than earlier in the year, indicating stable overcast conditions. While the surface observations showed only moderate and expected changes, the most notable changes were observed in the under-ice irradiance (Figures 6 and 7). Total transmitted irradiance decreased from  $7.5$  to  $2.6 \text{ W m}^{-2}$  (15–24 July) and further to  $0.6 \text{ W m}^{-2}$  on 10 August. This was related to a decrease in total transmittance from 0.049 to 0.010 (15–24 July). As a consequence, transmitted fluxes were only 40% of those during phase IVa. From 10 August onward, under-ice total irradiance increased again to  $6.3 \text{ W m}^{-2}$  (14 August),  $\sim 80\%$  of the level as before the drop on 15 July. This reincrease also changes the transmitted spectra back to the shape they had before the decrease on 15 July. At the same time, the wavelength of maximum transmit-

tance and the  $\tau(600)/\tau(450)$  ratio change back to values as they were at the end of phase III, before surface drainage. Figure 8c shows that the difference spectrum of transmittance ( $\tau(\lambda, t_1) - \tau(\lambda, t_2)$ ) between 2 July and 16 July is very similar to the one between 28 August and 25 July. The strong decrease of under-ice irradiance also indicates a maximum of total absorption in sea ice and uppermost ocean water of  $47 \text{ W m}^{-2}$ . Mean net flux into the surface was  $50 \text{ W m}^{-2}$ , 90% of the maximum during phase III. These observations are analyzed and discussed in detail in sections 4.2–4.4.

*Phase V: Autumn freezeup (15 August to 5 September):*

[46] On 15 August, total albedo started to increase from its minimum to values around 0.91, similar to those observed before melt onset. At the same time, total transmittance started to decrease and ended up at 0.029 at the end of the observation period (Figure 7a). These changes resulted from low air temperatures and the first new snow (afternoon of 14 August), as reported from the IMB. On the basis of these observations, 15 August may be defined as the end of melt season, after 66 days, and the transition from summer to autumn conditions. Also the  $\alpha(900)/\alpha(500)$  ratio increased again, pointing to less liquid water in the surface. The increase of albedo and decrease of transmittance were observed at all wavelengths, such that spectral shapes and absolute values after 31 August were almost identical to those before melt onset (phase I and Figure 8). The highest albedo, on 1 September, was measured during or shortly after a strong snowfall event that significantly increased snow thickness (Figure 4c). Hence, this spectrum might be biased by the snowfall itself, with accumulation on the incident sensor reducing the measured incident flux and leading to overestimates in albedo. However, subsequent measurements are reliable again, as the sensors were observed to be clean the next day. Incident (and reflected) irradiance was by far lowest during phase V. This resulted from low solar elevation angles (Figure 4d) and predominantly overcast conditions. As a consequence, net fluxes into and absorption by the snow and ice were also lowest. However, transmitted irradiance was significantly higher

than it was under higher solar irradiance in early summer (phase I and II), indicating continued relatively high transmittance values.

#### 4. Discussion

[47] Continuous and high temporal resolution measurements of spectral albedo and transmittance allow detailed descriptions and quantification of snow and sea-ice processes over different seasons. On the basis of the presented time series, it was possible to detect key events such as melt onset, melt-pond formation, surface drainage, duration of snow coverage, and autumn freezeup (Table 1). Furthermore, the vertical and spectral partitioning was quantified as a function of time, particularly interesting for under-ice irradiance, because such observations are still sparse. Beyond the standalone radiation measurements, the presented data show how additional observations of snow and sea-ice properties and mass balance increase the value of the radiation data and how a combined analysis results in more reliable and comprehensive results compared to a sum of single measurements. As integrative data sets are strongly needed to increase our understanding of atmosphere-ice-ocean interaction and to improve various numerical models, the results of this study might be of high interest for these applications.

[48] The presented data set is the first of its kind, and unlike earlier studies [Ehn *et al.*, 2008a; Light *et al.*, 2008; Perovich, 2005] it allows a detailed and combined analysis of the seasonality of albedo and transmittance. The strong seasonality of transmitted irradiance, which was found to be more complex than that of surface albedo, has not explicitly been observed before.

[49] This work represents the first seasonal application of the new station concept introduced by Nicolaus *et al.* [2010]. All irradiance measurements were obtained from the identical site for over 4 months without any gap in the time series or technical failures. This is most remarkable because autonomous (spectral) radiation measurements are technically and methodologically challenging, especially over long times and on sea ice.

##### 4.1. Seasonality of Albedo and Surface Fluxes

[50] The seasonality of total albedo shows principally the same characteristic five phases (Table 1) as described by Perovich *et al.* [2002a] and is illustrated by the photographs in Figure 3 and the corresponding spectra in Figure 8a. However, duration and timing of all phases were different from those at SHEBA, which was located between 76° and 80°N in the Beaufort and Chukchi seas (Beaufort Gyre) [Perovich *et al.*, 1999], while *Tara* drifted between 86° and 89°N through the Arctic Basin (Transpolar Drift, Figure 1).

[51] High solar elevation angles and high fractions of clear sky conditions led to the highest solar irradiance during phase II, which agrees with the analysis shown by Curry *et al.* [1996]. The next phase, phase III, was dominated by overcast conditions and mean irradiance was 25% lower (Table 2). One of the reasons for this change in cloud cover, possibly the dominating one, may have been the change from a snow-covered surface (phase II) to one with liquid water on it (phase III), which provided a large source of local moisture. However, large-scale advection of humid air masses

toward *Tara* could also have contributed to higher cloudiness. Although incident solar irradiance was reduced, a decrease in total albedo meant that phase III was characterized by the highest fluxes into the sea ice and the highest absorption in sea ice. Over the entire melting period, the IMB reported 0.53 m of surface and 0.10 m of bottom ablation. Hence, it may be concluded that the measured fluxes into the ice contributed mostly to surface and internal warming and melting, while ocean heat fluxes were comparably low.

[52] Melt onset (MO, 10 June) and freeze onset (FO, 15 August) were primarily defined on the basis of spectral albedo measurements and resulted in a melt season duration of 66 days. In a recent study, Markus *et al.* [2009] used daily brightness temperatures from passive microwave data to analyze MO and FO, dates after which continuous melting/freezing is observed, as well as early melt onset (EMO) and early freeze onset (EFO), dates after which first melt/freezing is observed, for different regions of the Arctic. For the region north of approximately 81°N, they determined that EMO occurred on 14 June, MO on 26 June, EFO on 15 September, and FO on 24 September 2007, all significantly later than the dates in this study (which are more comparable to their MO and FO than EMO and EFO). Differences in FO dates are especially large. While *Tara* was mostly north of the satellites' range (to 87.2°N), and comparisons must be performed with a region that extends much further south, various field studies have observed that the uppermost 10–20 cm of melt ponds were often frozen during September. In addition, Nicolaus *et al.* [2006] showed that regional variability of different melt season parameters is usually small in the Central Arctic. Both of these aspects indicate that FO dates and definitions from this study might be more reliable, especially for this high Arctic region.

[53] Figure 7a compares the total albedo from the spectral measurements with measurements of the true broadband albedo [Vihma *et al.*, 2008]. Both data sets show the same temporal evolution, but have a mean offset of  $0.11 \pm 0.05$ . The smallest differences occurred at the beginning and end of the observation period, when the surface was cold and dry (minimum offset was 0.01 on 19 May), while the largest differences occurred during the melting period when the surface was wet or even ponded (maximum offset was 0.23 on 16 July). Most differences are due to the shorter wavelength range of the spectral sensors, which do not observe wavelengths above 950 nm, where albedo is significantly lower, especially over wet surfaces and melt ponds. The shorter distance of the broadband radiometers to the nearby melt pond may also have affected the result, as neither data set is corrected for any melt-pond effect. Nevertheless, the correlation coefficient of both albedo time series is 0.95, showing that the presented spectral albedo data represent 90% of the variability within the broadband data. On this basis, the spectral data can be used to derive broadband values when real broadband measurements are not available or disturbed by sensor contamination [see also Nicolaus *et al.*, 2010]. In order to also match absolute values, known albedo values for given surface types, as for example optically thick new snow or the summer surface layer [e.g., Perovich *et al.*, 2007], may be used as anchor points. The other way around, using such anchor points of albedo for comparisons with

measured time series could reveal the effect of melt ponds or other surface features on the measured spectral data.

[54] The reflected irradiance was corrected for shadowing with a time- and wavelength-independent factor of 1.0769, a value determined from the geometry of the instrument setup with the assumption that the incident and reflected irradiance were completely isotropic at all times. This is certainly not entirely correct, but diffuse irradiance dominated the observation period. The selected procedure and given assumptions for the shadow correction [Nicolaus *et al.*, 2010] are similar to those applied by Brandt and Warren (personal communication, 2010), resulting in factors around 1.04 for a portable setup using a more advanced, but less robust spectroradiometer (Analytic Spectral Devices, Boulder, USA). In order to estimate uncertainties resulting from the shadow correction, shadow corrections were estimated for alternative solar irradiance conditions. For direct irradiance, the correction factor depends on solar azimuth and zenith angles. Solar zenith angles at times of highest solar elevation ranged from 65° to 80° and were mostly around 70° (Figure 4d). Shadow corrections for 100% direct irradiance from 70° and different azimuth angles range from 1.0574 to 1.0986. Shadow corrections for different zenith angles at the predominant azimuth angle are 1.1023 (60°) and 1.1067 (80°). More complex and time-dependent corrections could be applied using these different values, for example by combining different conditions weighted over time, but such an approach would risk introducing false signals. Finally, the range of these values suggests uncertainties in shadow corrections on the order of ±3%. This would affect all presented numbers that use the reflected irradiance (Tables 2 and 3), but not the general findings of this study.

#### 4.2. Seasonality of Transmittance and Absorbance

[55] One key result of this study is the characterization of the evolution of under-ice irradiance, based on the continuous time series. It was found that the general seasonality of transmittance is opposite that of albedo. This is not surprising, because less light reflected from the surface leaves more that can be transmitted deeper into and finally through the sea ice into the upper ocean. But on the basis of this similarity, it would have been expected that transmissivity increases after melt onset, remains at a high level, or even further increases, during summer, and decreases after the onset of freezing. However, the amount of transmitted irradiance decreased during the melting season (phase IV) almost to its spring level (phase I). This event and related processes are discussed in detail in section 4.3. As the under-ice sensor was located 1.4 m under the ice, changes in transmitted irradiance and transmittance do not exclusively describe changes in snow and sea-ice properties (transmittance of ice) but also include effects of the uppermost water layer, including biology therein. On the basis of absorption coefficients for seawater from literature [e.g., Wozniak and Dera, 2007], the estimated effect of the additional water column on the measured transmitted irradiance is a reduction of 20–30%, varying with time. Nevertheless, corrections for this distance have not been performed, because the time-variant spectral absorption coefficient is not known sufficiently well.

[56] Melt onset triggered a significant increase of total under-ice irradiance, at a rate of 0.52 W m<sup>-2</sup> per day during phases II and III, also confirming the result of Perovich [2005], that basically no light is transmitted during spring (here max. of phase I is 0.45 W m<sup>-2</sup>). The timing of this increase is of critical importance for biological processes in and under the ice [e.g., Arrigo, 2003; Lavoie *et al.*, 2005] and for modeling these processes [e.g., Jin *et al.*, 2006; Zeebe *et al.*, 1996]. This increase was accompanied by a shift in the wavelength of maximum transmittance from 500 to 520 nm and an increase of the  $\tau(600)/\tau(450)$  ratio (Figures 7d and 8b). Both features point to an increase of biomass in or directly beneath the sea ice [Ehn *et al.*, 2008a; Perovich *et al.*, 1993], beginning immediately after melt onset and continuing to its maximum in phase IVb. A similar result was found by applying the suggested [Mundy *et al.*, 2007] normalized difference index of 472 and 485 nm (data not shown here) to quantify biomass over the entire observation period. This supports the applicability of such difference indices for biomass estimation.

[57] The observed spectral shape of the under-ice irradiance (Figure 8b) is very similar to those measured by Ehn *et al.* [2008a], Perovich *et al.* [1993], and Perovich [1996]. In contrast, the spectral shape of transmittance shown by Light *et al.* [2008] is rather constant for wavelengths between 400 and 550 nm, except for one observation below FYI, which shows a maximum around 560 nm, similar to observations here, which they describe as an indication of absorption by chlorophyll *a* in the ice. These differences are difficult to examine and might be related to different surface, biological, or atmospheric conditions or to different measurement techniques.

[58] Comparisons of absolute irradiance with earlier studies are difficult because data sets often differ in observation time (season), region, and ice and snow properties. To focus on the effect of the ice, rather than seasonal, regional, or atmospheric differences, we compare transmittance rather than absolute irradiance measurements. The best comparable data set was measured during SHEBA [Light *et al.*, 2008]. The maximum transmittance of sea ice during SHEBA, measured under 2.18 m thick MYI with a surface scattering layer on 21 July 1998, was approximately 40% higher than the maximum during the drift of Tara (Figure 8, max. on 02 July). The main reason for this difference is probably biological activity, which strongly affected transmittance at our site during Phase IV, while the spectra of Light *et al.* [2008] did not indicate such activity, although measured at comparable times. Another factor is that the under-ice sensor in this study it was about 1.4 m under the ice, while Light *et al.* [2008] placed it much closer to the ice.

#### 4.3. Decrease of Transmitted Irradiance During the Melt Season

[59] The temporary decrease of transmitted irradiance and transmittance during the melt season is one of the most prominent features of the presented study and has not been observed and discussed in detail before. After its maximum on 02 July, transmitted irradiance decreased in two steps: First, during Phase IVa, by approximately 50% and afterward, during Phase IVb, by another 40% (of the maximum). After this, it increased again to its value at the end of Phase

IVa, before decreasing again after freeze onset. During Phase IVa the sea-ice surface drained, resulting in a surface scattering layer. This layer increased albedo, allowing less light to penetrate. But this process can only partially explain the decrease during Phase IVa, because the decrease in transmittance continued after the surface was drained (06 July), and the decrease changed the spectral shape significantly, which would not be expected from the change in surface conditions [Light *et al.*, 2008; Perovich, 1996]; the wavelength of maximum transmittance increased by 23 nm, and transmittance between 350 and 580 nm decreased significantly, while wavelengths larger than 600 nm were only weakly affected, and the  $\tau(600)/\tau(450)$  ratio increased. These results suggest biological activity was a strong contributor to the transmittance decrease during Phase IVa. Afterward, in Phase IVb, surface conditions did not change significantly and albedo decreased until freeze onset. The spectral shape of transmittance maintained approximately the same shape throughout Phase IVb. We suggest that during this time biological processes in ice and water were mainly responsible for the additional transmittance decrease, but the absorbing pigments did not change significantly. While we feel this is the best hypothesis to explain the observations, no observations of biomass or species composition are available and our conclusions are speculative.

[60] The rapid increase of transmittance between 10 and 15 August was most remarkable, returning the spectral shape and magnitude back to those seen in earlier observations in only five days, while the decrease extended over 41 days. Here we suggest that a change in ocean circulation washed most of the biomass away and/or changed the water mass properties in a way that caused the organisms to die and sink down. The main indication that this occurred is the rapid increase of drift velocity after 08 August (Figure 4e) together with increasing bottom ablation after 10 August. Together these could have removed parts of the porous ice matrix, where biomass is most abundant, and caused a freshening of the uppermost water layers. Furthermore, this hypothesis of changing drift patterns is consistent with observations of particularly strong ice motion in mid August. Before this episode, the 6-h mean drift speed of sea ice was between 0.05 and 0.10 m s<sup>-1</sup>; during the episode it increased to 0.15 to 0.35 m s<sup>-1</sup>. This episode was driven by a transient cyclone, formed over the Eurasian continent, which was passing south of *Tara*.

[61] On the basis of the high temporal resolution and large number of spectra, the presented data set could be used to derive the biomass in and under sea ice as a function of time. Methods are suggested and examples shown by Ehn *et al.* [2008a] and Mundy *et al.* [2007]. Furthermore, difference or absorption spectra, as presented in Figure 9, could be de-composed into known absorption spectra of various pigments [e.g., Ficek *et al.*, 2004, Figure 2a], aiming for analysis of pigment or even species composition. Such estimates are especially interesting as the method is non-destructive and does not need extensive sampling and analysis. A general and qualitative comparison of the difference spectra in Figure 9 and absorption spectra by Ficek *et al.* [2004] shows that the difference spectra match well with major absorption wavelengths of pigments, such as chlorophylls and carotenoids.

[62] Beside the detection of biomass, large amounts of biomass could affect measurements through bio fouling on sensor. This is also an aspect that can not be entirely excluded here, but no indication of fouling was found at sensor retrieval, and we are lacking a realistic explanation or mechanism for how to remove such growth in only a few days. Nevertheless, this possibility has to be considered for future applications of the presented setup [Nicolaus *et al.*, 2010].

#### 4.4. Vertical Partitioning of Solar Irradiance

[63] During the observation period from 29 April to 27 September, total (350 to 920 nm) incident, reflected, and transmitted energies were 1768, 1453, and 30 MJ m<sup>-2</sup>, respectively (Table 2). In total, 81% of solar irradiance was reflected, 17% absorbed by snow and sea ice, and 2% transmitted into the ocean. 95% of transmitted light was PAR. For comparison, during SHEBA, 68% of solar irradiance was reflected, 24% absorbed by snow and sea ice, and 8% transmitted into the ocean [Perovich, 2005], but comparing both sets of numbers is difficult because the SHEBA data are based on albedo measurements at 80 stations of different surface types and over a longer observation period during spring through autumn. SHEBA absorption and transmittance results are estimates from a radiative transfer model. The lower SHEBA albedo values result from the inclusion of melt-pond and open water surfaces. The larger estimated transmittances at SHEBA are due to thinner ice at SHEBA and to not including biological effects in the SHEBA radiative transfer modeling. Hence a decrease of transmitted irradiance due to primary production, as observed at *Tara*, was not included in the SHEBA analysis.

[64] Combining field measurements during SHEBA with the CCSM3 GCM model parameterization, Light *et al.* [2008] estimated that 3% of light would be transmitted through 3 m thick sea ice and 15% would be transmitted through 1 m thick sea ice, given the observed surface albedos between 0.77 and 0.81. Compared to this, lower total transmittance (2%) was measured at *Tara*, though ice conditions are within the given range. Again, the lower sensor height has a significant impact, as the signal is reduced by absorption and scattering in the uppermost water, especially during the phase when biomass significantly influences the spectra, after melt onset. Even considering this, our measurements show much lower transmittance than for the 1.3–1.9 m thick ice described by Light *et al.* [2008].

[65] The diagram in Figure 9 shows how the fraction of absorbed to transmitted irradiance changed with time. This comparison is of particular interest as it excludes the effect of surface albedo and highlights inner-ice and upper-ocean optical properties. During spring, only 1.5% of the total net flux into the surface was transmitted (phase I), but this fraction increased steadily to a maximum of 22.0% during autumn (phase V), except for the discussed decrease during Phase IV. Assuming most of the decrease during Phase IV was due to biomass in the ice and upper ocean, the decrease of this fraction during Phase IV is probably not representative of changes in the optical properties of the ice. Over the entire observation period, 8.6% of the total net flux into the ice (30 of 314 MJ m<sup>-2</sup>) is transmitted into the ocean and contributes to warming of the upper water layer and with this also indirectly to sea-ice bottom melt. The rest (284 MJ m<sup>-2</sup>)

is absorbed in the ice and directly used for internal warming and melting of snow and sea ice. Comparing this  $284 \text{ MJ m}^{-2}$  to the observed changes in snow and sea ice, only  $262 \text{ MJ m}^{-2}$  would be needed to explain these changes:  $68 \text{ MJ m}^{-2}$  to warm the sea ice to the melting point (see Figure 5),  $178 \text{ MJ m}^{-2}$  to melt  $0.6 \text{ m}$  of sea ice (Figure 4b), and  $16 \text{ MJ m}^{-2}$  to warm and melt  $0.15 \text{ m}$  snow (initial mean density and mean temperature were  $300 \text{ kg m}^{-3}$  and  $-13^\circ\text{C}$  (Figure 4c and unpublished snow pit data)). This balance neglects both absorption at wavelengths greater than  $950 \text{ nm}$  and sensible heat fluxes from the atmosphere and ocean. This seems to suggest that the measured absorption in snow and ice is overestimated, or that the observed changes of snow and sea ice are underestimated. This difference also points to the difficulties related to performing and relating both radiation and physical snow and sea-ice measurements in such a complex environment as drifting Arctic sea ice. Similar difficulties were also described by Nicolaus *et al.* [2009], although both studies were performed with a high degree of accuracy and care. However, we cannot expect to exactly close the energy balance as some of our absorbed energy was absorbed by the upper  $1.4 \text{ m}$  of ocean, not by ice or snow. In addition, small errors in the observations can have a significant effect on the net result (e.g., the extra  $22 \text{ MJ m}^{-2}$  represents just  $1.5\%$  of reflected energy, making errors in the shadow correction important).

[66] Assuming that under-ice irradiance was equal to the minimum in phase I before the observations started and to the minimum in phase V after the observations ended, we can estimate that  $63\%$  of the total transmitted solar energy reached the ocean during the 66-day-long melt season ( $\sim 1/6$  of the year), highlighting the strong seasonality of under-ice irradiance.

[67] Similarly, the effect of biomass on under-ice irradiance may be estimated by comparing the measured signal, including the strong decrease during phase IV, with an estimate of the under-ice irradiance time series without biological absorption. The latter is estimated by linearly interpolating the under-ice fluxes between the last measurement before the decrease and the first after the increase (17 July to 14 August). The total transmitted energy from this theoretical time series is 2.4 times as high as the measured signal ( $18.1$  vs.  $7.5 \text{ MJ m}^{-2}$ ). This change increases the mean transmittance by  $41\%$  from  $0.017$  to  $0.023$  and reduces the absorbed energy to a value closer to the estimate from snow and ice observations (see discussion above). If the difference of  $10.6 \text{ MJ m}^{-2}$  was used by biomass for photosynthesis, a photosynthetic efficiency of  $85\%$  [Zeebe *et al.*, 1996] results in  $9.0 \text{ MJ m}^{-2}$  being released again as heat from the organisms. This energy is therefore still available to warm the ocean or the ice or to contribute to bottom sea-ice melt of  $0.03 \text{ m}$ . These biological factors need to be considered when using these observations for other studies, e.g., in numerical models.

#### 4.5. Data Quality

[68] General aspects of data quality regarding the setup and sensors are discussed in Nicolaus *et al.* [2010]. This discussion also includes estimates of uncertainties and different sensor-specific issues. In order to present a high-quality data set that is most suitable to discuss seasonal changes, we focused on measurements during times of

highest solar elevation angles. Using data from local noon minimizes errors due to the imperfect cosine response of the sensors and reduces the effect of variable shadows and surface undulations, as conditions were observed under similar solar azimuth angles (floe rotation was not monitored and hence cannot be considered). The frequent cloud cover minimizes errors both due to the cosine response and due to any slight misleveling of the sensors. We tried to minimize uncertainties related to shadow corrections by formulating a rather complex correction procedure [Nicolaus *et al.*, 2010] that was applied in a simple manner in order to ease recalculations.

[69] One of the greatest uncertainties of the data set is the varying (both due to ice melt/growth and due to movement) distance of the under-ice sensor to the ice underside, making the differentiation of ice and water processes very difficult. The sensor was intentionally deployed below the bottom of the sea ice, so it did not freeze in during the expected bottom growth of ice thickness. This was done to prevent preferential ice growth on or around the sensor and rack. However, the final distance was greater than planned and resulted from inaccuracies during deployment. Additional uncertainties are introduced through the nearby melt pond, which was in the field of view of the sensors. As it changes surface albedo and transmittance, it has to be considered that the data do not describe a pure ice surface. Also the given wavelength range ( $320\text{--}950 \text{ nm}$ ) has to be taken into account when comparing with measurements of other sensor types or when using these data for other applications.

#### 4.6. Spatial Variability and Representativeness of Data

[70] Measuring the components of spectral solar radiation at the same piece of ice from spring through autumn is nondestructive and enables detailed process studies. As the station was drifting, some large-scale variability in atmospheric and radiative forcing is integrated during the observations, but this does not include any spatial variability of snow and ice properties on floe scales, including different features of the ice pack such as melt ponds, leads, or pressure ridges. In order to keep the optical site as undisturbed as possible, related measurements were performed on similar snow and ice conditions, but do include some spatial variability. Hence, for this method, it is important to choose a site for the station that is representative of the region.

[71] Repeated transects of ice thickness measurements in the *Tara* area confirm that the radiation and IMB sites represent modal ice conditions and that the temporal evolution of ice thickness at the site was representative of the region (C. Haas, personal communication, 2009), indicating these results should be representative of the larger area around *Tara*. It is also likely that these data are generally representative of multiyear ice with similar thicknesses of snow and sea ice. Other snow and ice regimes may show different results, especially regarding under-ice irradiance. The presented albedo and transmission values are not meant to be representative of the floe-average values as they do not include a sample of the different surface types on the flow. During the dry and wet snow phases, the surface was relatively homogeneous, but once melt ponds formed, our data are representative of the surface types in the small areas seen by the sensors: mostly bare ice for albedo, and a (not

necessarily representative) mixture of bare ice and melt pond for transmittance.

[72] Even though the *Tara* data were gathered prior to the sea-ice extent minimum in 2007, it is likely that the results are characteristic for similar ice conditions in other years, as well. The main retreat was observed in the East Siberian and Laptev seas, while ice concentration in the study area was not exceptional [e.g., *Stroeve et al.*, 2008]. *Markus et al.* [2009] found that melt onset in the study region in 2007 was very close to the long-term mean, but freeze onset happened much later than the mean since 1979. But their dates could not be confirmed by the presented in situ measurements. Furthermore, the atmospheric forcing at *Tara* was not exceptional, compared to data from the Russian North Pole stations, which covered similar regions of the Arctic Basin [*Vihma et al.*, 2008]. IMB data gathered north of Greenland in 2007 [*Perovich et al.*, 2008] show similar characteristics of surface and bottom ablation to those at *Tara*.

[73] Although the observed decrease of transmittance was not explicitly observed before, some aspects were quantitatively described earlier [*Ehn et al.*, 2008a; *Mundy et al.*, 2007; *Perovich et al.*, 1993]. Hence, we think that the phases described here may be generalized for Arctic sea ice. However, it needs to be considered that the intensity of biological processes varies strongly in different regions [*Carmack et al.*, 2006], and in regions with low biological activity the observed effect during phase IV might be significantly lower, if present at all, allowing higher transmittance. Furthermore, in other regions, especially those close to shore, sediments in the ice and in the water, as well as large amounts of organic matter, may reduce under-ice irradiance more than biological activity may [*Light et al.*, 2008; *Perovich et al.*, 1998].

## 5. Conclusions and Perspectives

[74] Using a modern setup of spectral radiometers above and under sea ice, the most comprehensive time series of spectral albedo and transmittance was gathered during the drift of *Tara* through the Transpolar Drift. As the data set covers most of the sunlit part of the year and includes the key melt and freeze periods, it was possible to describe the seasonal evolution of physical, optical, and some biological processes of snow and sea ice, including quantification of melt onset, melt season duration, and freeze onset, which are critical parameters in climate models. It was also possible to explain 90% of the temporal variability of broadband albedo based on the spectral data set of reduced wavelength range (320–950 nm).

[75] The presented combination of spectral radiation and ice mass balance studies allows a qualitative and quantitative description of snow and sea-ice processes, even with minimal additional in situ observations. Biological studies would benefit from quantifying spectral fluxes into the bottom ice layers and into the upper ocean, allowing estimates of biomass or even species composition based on known absorption spectra of different pigments.

[76] The presented setup can be further developed toward an independent buoy system, sending its data via satellite in real time [see also *Nicolaus et al.*, 2010]. As can be seen from this study, such a station would be most beneficial

when deployed together with an IMB. However, the presented data also point to the need for including horizontal transects or additional sensors to quantify spatial variability on different scales. This spatial extension could be realized on floe to regional scales by manual and autonomous measurements using autonomous underwater vehicles and unmanned aerial vehicles. Beyond this, on larger scales, these data are well suited to be combined with high-resolution optical satellite data (e.g., moderate resolution imaging spectro-radiometer), taking advantage of the high spectral resolution.

[77] The comprehensive data set could be most valuable to further develop and improve optical models for snow and sea ice. Using different parts of the data set as forcing data, numerical studies with one-dimensional models such as SNTherm [*Andreas et al.*, 2004; *Jordan et al.*, 1999; *Nicolaus et al.*, 2006] and HIGHSEA [*Cheng et al.*, 2003, 2008; *Launiainen and Cheng*, 1998] might help us to understand snow and sea-ice processes in even more detail and to derive additional quantities that were not measured in situ. Using radiative transfer models, inherent optical properties of the sea ice at *Tara* could be derived [*Hamre et al.*, 2004; *Stamnes et al.*, 1988], allowing further comparison with related studies. Other future work with the data could focus on improving albedo schemes in regional to global models [e.g., *Pedersen and Winther*, 2005] and improving the forcing for biological models in the Arctic Ocean.

[78] **Acknowledgments.** We strongly acknowledge the support of the *Tara* Arctic project, which enabled these measurements in the high Arctic, and especially thank the *Tara* summer crew for maintaining the radiation station and performing all additional snow and sea-ice measurements. Great thanks to Timo Palo (University of Tartu, Estonia, and *Tara* crew), who performed most of the measurements and was heavily involved in all in situ observations, including documentation and photography. Furthermore, we are grateful to all other colleagues who supported our field measurements at *Tara* with a lot of helping hands. We thank Timo Vihma (Finnish Meteorological Institute) and the University of Tartu for providing the meteorological and broadband irradiance data and for fruitful discussions about these data sets. Stephen Warren (University of Washington, USA) and one anonymous reviewer gave most constructive comments, helping us improving the manuscript. We greatly appreciate their contribution. Anja Nicolaus helped preparing the thin sections of the ice core. This study was funded through the Developing Arctic Modeling and Observing Capabilities for Long-Term Environmental Studies (DAMOCLES) project, which is financed by the European Union. Manuscript preparation was supported through a Leiv Eiriksson stipend from the Research Council of Norway (project 192516) for Marcel Nicolaus. Additional funding was received from the IPY project iAOS Norway-Closing the Loop, the Research Council of Norway (grant 176096/S30), and the internal funds of the Norwegian Polar Institute and its Centre for Ice, Climate, and Ecosystems (ICE).

## References

- Andreas, E. L., R. E. Jordan, and A. P. Makshtas (2004), Simulations of snow, ice, and near-surface atmospheric processes on Ice Station Weddell, *J. Hydrometeorol.*, 5(4), 611–624.
- Aoki, T., M. Fukabori, A. Hachikubo, Y. Tachibana, and F. Nishio (2000), Effects of snow physical parameters on spectral albedo and bidirectional reflectance of snow surface, *J. Geophys. Res.*, 105(D8), 10,219–10,236, doi:10.1029/1999JD901122.
- Aoki, T., A. Hachikubo, and M. Hori (2003), Effects of snow physical parameters on shortwave broadband albedos, *J. Geophys. Res.*, 108(D19), 4616, doi:10.1029/2003JD003506.
- Arrigo, K. R. (2003), Primary production in sea ice, in *Sea ice—An Introduction to Its Physics, Biology, Chemistry, and Geology*, edited by D. N. Thomas and G. S. Dieckmann, pp. 143–183, Blackwell Sci., Oxford.
- Baker, D. G., R. H. Skaggs, and D. L. Ruschy (1991), Snow depth required to mask the underlying surface, *J. Appl. Meteorol.*, 30(3), 387–392.

- Bohren, C. F., and B. R. Barkstrom (1974), Theory of the optical properties of snow, *J. Geophys. Res.*, *79*(30), 4527–4535, doi:10.1029/JC079i030p04527.
- Brandt, R. E., S. G. Warren, A. P. Worby, and T. C. Grenfell (2005), Surface albedo of the Antarctic sea ice zone, *J. Clim.*, *18*(17), 3606–3622.
- Carmack, E., D. Barber, J. Christensen, R. Macdonald, B. Rudels, and E. Sakshaug (2006), Climate variability and physical forcing of the food webs and the carbon budget on panarctic shelves, *Prog. Oceanogr.*, *71*(2–4), 145–181.
- Cheng, B., J. Launianen, and T. Vihma (2003), Modelling of superimposed ice formation and sub-surface melting in the Baltic Sea, *Geophysica*, *39*(1–2), 31–50.
- Cheng, B., Z. Zhang, T. Vihma, M. M. Johansson, L. Bian, Z. Li, and H. Wu (2008), Model experiments on snow and ice thermodynamics in the Arctic Ocean with CHINARE 2003 data, *J. Geophys. Res.*, *113*, C09020, doi:10.1029/2007JC004654.
- Comiso, J. C., C. L. Parkinson, R. Gersten, and L. Stock (2008), Accelerated decline in the Arctic sea ice cover, *Geophys. Res. Lett.*, *35*, L01703, doi:10.1029/2007GL031972.
- Curry, J. A., W. B. Rossow, D. Randall, and J. L. Schramm (1996), Overview of Arctic cloud and radiation characteristics, *J. Clim.*, *9*(8), 1731–1764.
- Curry, J. A., J. L. Schramm, D. K. Perovich, and J. O. Pinto (2001), Applications of SHEBA/FIRE data to evaluation of snow/ice albedo parameterizations, *J. Geophys. Res.*, *106*(D14), 15,345–15,355, doi:10.1029/2000JD900311.
- Ehn, J. K., C. J. Mundy, and D. G. Barber (2008a), Bio-optical and structural properties inferred from irradiance measurements within the bottom-most layers in an Arctic landfast sea ice cover, *J. Geophys. Res.*, *113*, C03S03, doi:10.1029/2007JC004194.
- Ehn, J. K., T. N. Papakyriakou, and D. G. Barber (2008b), Inference of optical properties from radiation profiles within melting landfast sea ice, *J. Geophys. Res.*, *113*, C09024, doi:10.1029/2007JC004656.
- Fetterer, F., and N. Untersteiner (1998), Observations of melt ponds on Arctic sea ice, *J. Geophys. Res.*, *103*(C11), 24,821–24,835, doi:10.1029/98JC02034.
- Ficek, D., S. Kaczmarek, J. Ston-Egiert, B. Wozniak, R. Majchrowski, and J. Dera (2004), Spectra of light absorption by phytoplankton pigments in the Baltic; conclusions to be drawn from a Gaussian analysis of empirical data, *Oceanologia*, *46*(4), 533–555.
- Gascard, J.-C., et al. (2008), Exploring Arctic Transpolar Drift during dramatic sea ice retreat, *Eos Trans. AGU*, *89*(3), 21–28, doi:10.1029/2008EO030001.
- Giles, K. A., S. W. Laxon, and A. L. Ridout (2008), Circumpolar thinning of Arctic sea ice following the 2007 record ice extent minimum, *Geophys. Res. Lett.*, *35*, L22502, doi:10.1029/2008GL035710.
- Grenfell, T. C., and G. A. Maykut (1977), The optical properties of ice and snow in the Arctic basin, *J. Glaciol.*, *18*, 445–463.
- Grenfell, T. C., and D. K. Perovich (1984), Spectral albedos of sea ice and incident solar irradiance in the southern Beaufort Sea, *J. Geophys. Res.*, *89*(C3), 3573–3580, doi:10.1029/JC089iC03p03573.
- Grenfell, T. C., B. Light, and D. K. Perovich (2006), Spectral transmission and implications for the partitioning of shortwave radiation in arctic sea ice, *Ann. Glaciol.*, *44*, 1–6.
- Haas, C., A. Pfaffling, S. Hendricks, L. Rabenstein, J.-L. Etienne, and I. Rigor (2008), Reduced ice thickness in Arctic Transpolar Drift favors rapid ice retreat, *Geophys. Res. Lett.*, *35*, L17501, doi:10.1029/2008GL034457.
- Hamre, B., J.-G. Winther, S. Gerland, J. J. Stamnes, and K. Stamnes (2004), Modeled and measured optical transmittance of snow-covered first-year sea ice in Kongsfjorden, Svalbard, *J. Geophys. Res.*, *109*, C10006, doi:10.1029/2003JC001926.
- Jin, M., C. J. Deal, J. Wang, K.-H. Shin, N. Tanaka, T. E. Whitley, S. H. Lee, and R. R. Gradinger (2006), Controls of the landfast ice-ocean ecosystem offshore Barrow, Alaska, *Ann. Glaciol.*, *44*, 63–72.
- Jordan, R. E., E. L. Andreas, and A. P. Makshtas (1999), Heat budget of snow-covered sea ice at North Pole 4, *J. Geophys. Res.*, *104*(C4), 7785–7806, doi:10.1029/1999JC900011.
- Kwok, R., and D. A. Rothrock (2009), Decline in Arctic sea ice thickness from submarine and ICESat records: 1958–2008, *Geophys. Res. Lett.*, *36*, L15501, doi:10.1029/2009GL039035.
- Launianen, J., and B. Cheng (1998), Modelling of ice thermodynamics in natural water bodies, *Cold Reg. Sci. Technol.*, *27*, 153–178.
- Lavoie, D., K. Denman, and C. Michel (2005), Modeling ice algal growth and decline in a seasonally ice-covered region of the Arctic (Resolute Passage, Canadian Archipelago), *J. Geophys. Res.*, *110*, C11009, doi:10.1029/2005JC002922.
- Legendre, L., and M. Gosselin (1991), In situ spectroradiometric estimation of microalgal biomass in first-year sea ice, *Polar Biol.*, *11*(2), 113–115.
- Light, B., T. C. Grenfell, and D. K. Perovich (2008), Transmission and absorption of solar radiation by Arctic sea ice during the melt season, *J. Geophys. Res.*, *113*, C03023, doi:10.1029/2006JC003977.
- Markus, T., J. C. Stroeve, and J. Miller (2009), Recent changes in Arctic sea ice melt onset, freezeup, and melt season length, *J. Geophys. Res.*, *114*, C12024, doi:10.1029/2009JC005436.
- Maslanik, J. A., C. Fowler, J. Stroeve, S. Drobot, J. Zwally, D. Yi, and W. Emery (2007), A younger, thinner Arctic ice cover: Increased potential for rapid, extensive sea-ice loss, *Geophys. Res. Lett.*, *34*, L24501, doi:10.1029/2007GL032043.
- Maykut, G. A., and T. C. Grenfell (1975), The spectral distribution of light beneath first-year sea ice in the Arctic Ocean, *Limnol. Oceanogr.*, *20*(4), 554–563.
- Morassutti, M. P. (1991), Climate model sensitivity to sea ice albedo parameterization, *Theor. Appl. Climatol.*, *44*(1), 25–36.
- Mundy, C. J., J. K. Ehn, D. G. Barber, and C. Michel (2007), Influence of snow cover and algae on the spectral dependence of transmitted irradiance through Arctic landfast first-year sea ice, *J. Geophys. Res.*, *112*, C03007, doi:10.1029/2006JC003683.
- Nghiem, S. V., I. G. Rigor, D. K. Perovich, P. Clemente-Colón, J. W. Weatherly, and G. Neumann (2007), Rapid reduction of Arctic perennial sea ice, *Geophys. Res. Lett.*, *34*, L19504, doi:10.1029/2007GL031138.
- Nicolaus, M., C. Haas, J. Bareiss, and S. Willmes (2006), A model study of differences of snow thinning on Arctic and Antarctic first-year sea ice during spring and summer, *Ann. Glaciol.*, *44*, 147–153.
- Nicolaus, M., C. Haas, and S. Willmes (2009), Evolution of first-year and second-year snow properties on sea ice in the Weddell Sea during spring-summer transition, *J. Geophys. Res.*, *114*, D17109, doi:10.1029/2008JD011227.
- Nicolaus, M., S. R. Hudson, S. Gerland, and K. Munderloh (2010), A modern concept for autonomous and continuous measurements of spectral albedo and transmittance of sea ice, *Cold Reg. Sci. Technol.*, *62*(1), 14–28.
- Parkinson, C. L., and D. J. Cavalieri (2008), Arctic sea ice variability and trends, 1979–2006, *J. Geophys. Res.*, *113*, C07003, doi:10.1029/2007JC004558.
- Pedersen, C. A., and J. G. Winther (2005), Intercomparison and validation of snow albedo parameterization schemes in climate models, *Clim. Dyn.*, *25*(4), 351–362.
- Perovich, D. K. (1996), The optical properties of sea ice, *Monograph 96-1*, CRREL, Hanover, N. H.
- Perovich, D. K. (2005), On the aggregate-scale partitioning of solar radiation in Arctic sea ice during the Surface Heat Budget of the Arctic Ocean (SHEBA) field experiment, *J. Geophys. Res.*, *110*, C03002, doi:10.1029/2004JC002512.
- Perovich, D. K., G. F. Cota, G. A. Maykut, and T. C. Grenfell (1993), Biooptical observations of first-year Arctic sea ice, *Geophys. Res. Lett.*, *20*(11), 1059–1062, doi:10.1029/93GL01316.
- Perovich, D. K., C. S. Roesler, and W. S. Pegau (1998), Variability in Arctic sea ice optical properties, *J. Geophys. Res.*, *103*(C1), 1193–1208, doi:10.1029/97JC01614.
- Perovich, D. K., et al. (1999), Year on ice gives climate insights, *Eos Trans. AGU*, *80*(41), 485–486.
- Perovich, D. K., T. C. Grenfell, B. Light, and P. V. Hobbs (2002a), Seasonal evolution of the albedo of multiyear Arctic sea ice, *J. Geophys. Res.*, *107*(C10), 8044, doi:10.1029/2000JC000438.
- Perovich, D. K., W. B. Tucker III, and K. A. Ligett (2002b), Aerial observations of the evolution of ice surface conditions during summer, *J. Geophys. Res.*, *107*(C10), 8048, doi:10.1029/2000JC000449.
- Perovich, D. K., T. C. Grenfell, J. A. Richter-Menge, B. Light, W. B. Tucker III, and H. Eicken (2003), Thin and thinner: Sea ice mass balance measurements during SHEBA, *J. Geophys. Res.*, *108*(C3), 8050, doi:10.1029/2001JC001079.
- Perovich, D. K., S. V. Nghiem, T. Markus, and A. Schweiger (2007), Seasonal evolution and interannual variability of the local solar energy absorbed by the Arctic sea ice-ocean system, *J. Geophys. Res.*, *112*, C03005, doi:10.1029/2006JC003558.
- Perovich, D. K., J. A. Richter-Menge, K. F. Jones, and B. Light (2008), Sunlight, water, and ice: Extreme Arctic sea ice melt during the summer of 2007, *Geophys. Res. Lett.*, *35*, L11501, doi:10.1029/2008GL034007.
- Rampal, P., J. Weiss, and D. Marsan (2009), Positive trend in the mean speed and deformation rate of Arctic sea ice, 1979–2007, *J. Geophys. Res.*, *114*, C05013, doi:10.1029/2008JC005066.
- Richter-Menge, J., D. K. Perovich, B. C. Elder, K. Claffey, I. Rigor, and M. Ortmeier (2006), Ice mass-balance buoys: A tool for measuring and attributing changes in the thickness of the Arctic sea-ice cover, *Ann. Glaciol.*, *44*, 205–210.

- Sankelo, P., J. Haapala, I. Heiler, and E. Rinne (2010), Melt pond formation and temporal evolution at the drifting station Tara during summer 2007, *Polar Res*, in press.
- Stamnes, K., S. C. Tsay, W. Wiscombe, and K. Jayaweera (1988), Numerically stable algorithm for discrete-ordinate-method radiative-transfer in multiple-scattering and emitting layered media, *Appl. Opt.*, 27(12), 2502–2509.
- Stroeve, J. C., M. M. Holland, W. Meier, T. Scambos, and M. Serreze (2007), Arctic sea ice decline: Faster than forecast, *Geophys. Res. Lett.*, 34, L09501, doi:10.1029/2007GL029703.
- Stroeve, J. C., M. Serreze, S. Drobot, S. Gearheard, M. Holland, J. Maslanik, W. Meier, and T. Scambos (2008), Arctic sea ice extent plummets in 2007, *Eos Trans. AGU*, 89(2), 13–20, doi:10.1029/2008EO020001.
- Vihma, T., J. Jaagus, E. Jakobson, and T. Palo (2008), Meteorological conditions in the Arctic Ocean in spring and summer 2007 as recorded on the drifting ice station Tara, *Geophys. Res. Lett.*, 35, L18706, doi:10.1029/2008GL034681.
- Wang, M. Y., and J. E. Overland (2009), A sea ice free summer Arctic within 30 years?, *Geophys. Res. Lett.*, 36, L07502, doi:10.1029/2009GL037820.
- Warren, S. G. (1982), Optical properties of snow, *Rev. Geophys. Space Phys.*, 20(1), 67–89.
- Weeks, W. F., and S. F. Ackley (1986), The growth, structure and properties of sea ice, in *The Geophysics of Sea Ice*, edited by N. Untersteiner, pp. 9–164, Plenum Press, New York.
- Wozniak, B., and J. Dera (2007), *Light Absorption of Sea Water*, 463 pp., Springer, Berlin.
- Zeebe, R. E., H. Eicken, D. H. Robinson, D. WolfGladrow, and G. S. Dieckmann (1996), Modeling the heating and melting of sea ice through light absorption by microalgae, *J. Geophys. Res.*, 101(C1), 1163–1181, doi:10.1029/95JC02687.
- 
- S. Gerland and S. R. Hudson, Norwegian Polar Institute, Polar Environmental Centre, 9296 Tromsø, Norway.
- J. Haapala, Finnish Meteorological Institute, Erik Palménin aukio 1, 00560 Helsinki, Finland.
- S. Hanson, Danish Meteorological Institute, Lyngbyvejen 100, 2100 Copenhagen, Denmark.
- M. Nicolaus, Alfred Wegener Institute for Polar and Marine Research, Bussestr., 24, 27570 Bremerhaven, Germany. (marcel.nicolaus@awi.de)
- D. K. Perovich, Cold Regions Research and Engineering Laboratory, 72 Lyme Rd., Hanover, NH 03755-1290, USA.